https://doi.org/10.5194/egusphere-2026-4324
Preprint. Discussion started: 13 August 2026

Initial generation and validation of the JAXA four-sensor synergy radiation budget product (ALL_RAD) for the EarthCARE mission

Takashi M. Nagao[1], Kentaroh Suzuki[2], Akira Yamauchi[3], Eiji Oikawa[1], Miho Sekiguchi[4], Haruma Ishida[2], and Masataka Muto[3]

[1]Meteorological Research Institute, Japan Meteorological Agency, Tsukuba, Japan
[2]Atmosphere and Ocean Research Institute, The University of Tokyo, Kashiwa, Japan
[3]Japan Aerospace Exploration Agency, Tsukuba, Japan
[4]Faculty of Marine Technology, Tokyo University of Marine Science and Technology, Tokyo, Japan

Correspondence to: Takashi M. Nagao (tmnagao@mri-jma.go.jp)

Abstract.
The Earth Cloud, Aerosol and Radiation Explorer (EarthCARE) mission provides an unprecedented opportunity to investigate the Earth's radiation budget using synergistic observations from active and passive sensors. In this study, we present the development and validation of the JAXA four-sensor synergy radiation budget product (ALL_RAD), version Ba, which was publicly released on 1 December 2025. The ALL_RAD algorithm generates composite cloud and aerosol profiles by integrating Level-2 retrieval products from the Cloud Profiling Radar (CPR), the Atmospheric Lidar (ATLID), and the Multi-Spectral Imager (MSI), and then estimates broadband shortwave and longwave radiative fluxes and heating rate profiles using a one-dimensional radiative transfer model. The performance of ALL_RAD is evaluated against the ESA radiative flux product (BMA-FLX) derived from broadband radiometer (BBR) observations. The comparison shows substantial improvements in radiative flux estimates relative to earlier pre-launch evaluations, with instantaneous shortwave bias and root-mean-square error (RMSE) reduced to −0.6 and 33.7 W m^{-2}, respectively, and the longwave bias and RMSE reduced to +2.2 and 8.1 W m^{-2}, respectively. In addition, comparisons with ground-based observations from the Baseline Surface Radiation Network (BSRN) demonstrate good agreement for both shortwave and longwave surface fluxes. The physical consistency of the product is further assessed using cloud radiative effects and associated heating rate profiles as well as aerosol radiative effects, which are found to be broadly consistent with previous studies using A-Train observations. Future work will extend the validation to longer periods and broader cloud regimes, and will further assess uncertainty sources related to aerosol representation, spatial representativeness, and three-dimensional radiative effects. Overall, ALL_RAD provides a reliable basis for estimating EarthCARE radiative fluxes and derived quantities, thus establishing a foundation for radiative closure studies using EarthCARE observations.

https://doi.org/10.5194/egusphere-2026-4324
Preprint. Discussion started: 13 August 2026

1 Introduction

The Earth's radiation budget plays a fundamental role in regulating the climate system by controlling the balance between incoming solar radiation and outgoing terrestrial radiation. Changes in the planet's radiation balance can affect atmospheric circulation patterns (Hartmann and Short, 1980; Liebmann and Hartmann, 1982). The interaction of clouds and aerosols with radiation exerts a significant influence on this balance, yet they remain one of the largest sources of uncertainty in climate studies (IPCC, 2023). Precise estimation of their radiative effects therefore requires observational constraints that encompass both their vertical structure and horizontal variability. Satellite observations have been essential for providing global coverage of these properties, thereby forming the basis for our current understanding of cloud–radiation and aerosol–radiation interactions, particularly when combining complementary observations from multiple sensors (e.g., Stephens et al., 2012; Stephens et al., 2015).

The A-Train satellite constellation has demonstrated the value of synergistic observations from active and passive sensors for characterizing clouds, aerosols, and their radiative effects. In particular, the combination of radar and lidar measurements from CloudSat and CALIPSO, together with passive observations from MODIS and broadband radiative flux measurements from CERES, has enabled significant advances in our understanding of cloud vertical structure and its radiative impacts (e.g., L'Ecuyer et al., 2015; Stephens et al., 2018). The integration of these multi-sensor observations has led to the development of merged datasets that combine cloud, aerosol, and radiative flux information within a consistent framework, including products such as the CERES–CALIPSO–CloudSat–MODIS (CCCM) dataset (Kato et al., 2011; Ham et al., 2017) and CloudSat radiative flux products (2B-FLXHR and 2B-FLXHR-LIDAR; L'Ecuyer et al., 2008; Henderson et al., 2013). These datasets enable detailed investigation of cloud radiative effects and their vertical structure, including radiative heating rate profiles (e.g., Kato et al., 2018). They have also been widely used to quantify the radiative impacts of cloud properties on the Earth's radiation budget, including the effects of cloud phase and multilayer cloud structures (Luo et al., 2017; Matus and L'Ecuyer, 2017). Multi-sensor observations are also essential for understanding aerosol radiative effects, particularly through their vertical distribution and interactions with clouds (Oikawa et al., 2013, 2018; Matus et al., 2019). In these studies, top-of-atmosphere (TOA) radiative fluxes measured by CERES have served as an essential reference for constraining and evaluating radiative flux estimates derived from multi-sensor observations (Loeb et al., 2018, 2024). These advances underscore the importance of synergistic multi-sensor observations for constraining cloud–aerosol–radiation interactions.

Building on these advances, the Earth Cloud, Aerosol and Radiation Explorer (EarthCARE) mission provides a new opportunity to further constrain cloud–aerosol–radiation interactions through synergistic observations from active and passive sensors (Illingworth et al., 2015; Wehr et al., 2023). Unlike the A-Train constellation, where measurements from different instruments are not strictly co-located in space and time, EarthCARE is specifically designed to acquire co-registered observations from four instruments: the Cloud Profiling Radar (CPR), the Atmospheric Lidar (ATLID), the Multi-Spectral Imager (MSI), and the Broadband Radiometer (BBR). This configuration enables a more consistent characterization of cloud and aerosol properties together with coincident measurements of TOA radiative fluxes. A key objective of the EarthCARE

https://doi.org/10.5194/egusphere-2026-4324
Preprint. Discussion started: 13 August 2026

mission is to achieve radiative closure, i.e., to reconcile radiative fluxes derived from cloud and aerosol properties retrieved from CPR, ATLID and MSI with those directly observed by the BBR. This enables the derivation of physically consistent pairs of cloud and aerosol vertical structures and their associated radiative properties, constrained by both active and passive observations and consistent with TOA radiative flux measurements.

In this context, the EarthCARE mission includes the development of radiation products by both ESA and JAXA (Eisinger et al., 2024), reflecting complementary approaches to achieving radiative closure. Alongside the ESA radiation product ACM-RT (Cole et al., 2023), the JAXA four-sensor synergy radiation budget product (ALL_RAD) has been developed within this framework to provide radiative fluxes and heating rate profiles based on the synergistic use of JAXA Level-2 cloud and aerosol retrieval products. ALL_RAD is designed to exploit the co-registered observations unique to EarthCARE to achieve improved radiative consistency between retrieved atmospheric properties and observed radiative fluxes.

In this study, we present the production and validation of ALL_RAD version Ba, which was publicly released on 1 December 2025, and evaluate its performance in terms of radiative flux accuracy. The overall framework of the ALL_RAD algorithm follows the approach described in Yamauchi et al. (2024), with adaptations for the updated JAXA Level-2 retrieval products. The algorithm first constructs composite vertical profiles of clouds and aerosols by integrating retrievals from CPR, ATLID, and MSI. These retrievals are based on JAXA Level-2 products, including AC_CLP (Sato et al., 2025), ATL_CLA (Nishizawa et al., 2026), and MSI_CLP (Wang et al., 2023). The resulting composite profiles are then used as input to the one-dimensional radiative transfer model MstrnX (Nakajima et al., 2000; Sekiguchi and Nakajima, 2008) to estimate broadband shortwave and longwave radiative fluxes at the TOA, in the atmosphere, and at the surface, as well as the corresponding radiative heating rate profiles. This one-dimensional, rather than three-dimensional, radiative transfer calculation is a practical design choice to meet the latency requirements for the operational flux estimation process of the JAXA standard product in the EarthCARE mission. Within this radiative transfer framework, the algorithm computes radiative fluxes under four atmospheric conditions: all-sky, clear-sky without clouds but with aerosols, cloudy-sky without aerosols but with clouds, and pristine-sky without clouds and aerosols. These calculations are used to separately quantify the radiative effects of clouds and aerosols.

To evaluate the performance of ALL_RAD version Ba, we compare the estimated radiative fluxes with independent reference datasets. At the TOA, the fluxes are compared with the BMA-FLX product (Velázquez Blázquez et al., 2024b), which is derived from broadband multi-angle measurements by the BBR instrument, to assess the accuracy of the TOA radiative flux estimates. In addition, although the available data are limited, surface radiative fluxes are compared with ground-based observations from the Baseline Surface Radiation Network (BSRN; Ohmura et al., 1998). Together with the TOA comparison, this provides an initial step toward radiative closure assessment by evaluating radiative fluxes at both TOA and surface, thereby serving as a basis for better quantification of radiative energy partitioning into atmosphere and surface. This evaluation framework provides a broader assessment of the radiative consistency of the ALL_RAD product.

The remainder of this paper is organized as follows. Section 2 describes the ALL_RAD algorithm, input data, output variables, and data processing framework. Section 3 presents the all-sky TOA radiative flux evaluation against the BBR-derived BMA-FLX product. Section 4 evaluates clear-sky TOA radiative fluxes against BMA-FLX, and Section 5 evaluates

https://doi.org/10.5194/egusphere-2026-4324
Preprint. Discussion started: 13 August 2026

surface radiative fluxes using ground-based BSRN observations. Section 6 discusses the physical consistency of derived radiative quantities, such as cloud and aerosol radiative effects, and remaining uncertainties. Finally, Section 7 presents the conclusions.

2 ALL_RAD algorithm and data processing framework

In this section, we describe the overall framework of the ALL_RAD algorithm and the associated data processing procedure. The ALL_RAD algorithm, including the construction of composite cloud and aerosol profiles and the radiative transfer calculations described in the following subsections, is implemented based on Yamauchi et al. (2024), with adaptations to account for the characteristics of the input products and the requirements of the ALL_RAD output variables.

2.1 Input data: JAXA Level-2 products

This subsection describes the JAXA Level-2 cloud and aerosol retrieval products used as input to the ALL_RAD algorithm. Figure 1 provides a schematic overview of the ALL_RAD processing framework, showing how EarthCARE sensor observations are connected to the corresponding JAXA Level-2 retrieval products and subsequently used as input to the ALL_RAD algorithm. The figure also indicates the comparison with the ESA BMA-FLX product.

https://doi.org/10.5194/egusphere-2026-4324
Preprint. Discussion started: 13 August 2026

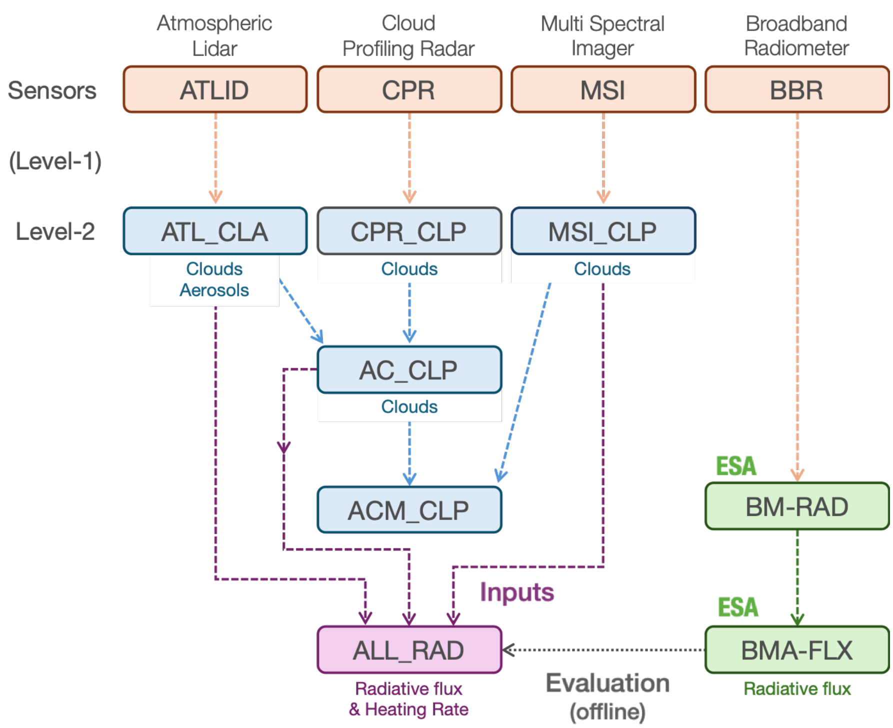

Figure 1. Schematic overview of the ALL_RAD processing framework and its comparison with BMA-FLX. The figure illustrates the relationship between the EarthCARE sensors and the corresponding JAXA Level-2 retrieval products, and the subsequent ALL_RAD algorithm. The ESA BMA-FLX product is shown as an independent reference for evaluating ALL_RAD TOA radiative fluxes. For clarity, intermediate Level-1 product names are omitted, and only the processing steps relevant to ALL_RAD are shown.

The ALL_RAD algorithm utilizes retrieval products derived from ATLID, CPR, and MSI, as well as combined products that exploit their synergistic observations. Specifically, the algorithm uses the following JAXA Level-2 products:

- ATL_CLA: a cloud and aerosol product providing vertically resolved cloud and aerosol properties retrieved from ATLID measurements (Nishizawa et al., 2026).
- AC_CLP: a combined ATLID–CPR cloud product providing vertically resolved cloud properties retrieved from synergistic radar and lidar observations (Sato et al., 2025). The product is generated by combining retrievals from CPR_CLP, a CPR-only cloud product, with complementary cloud information provided by ATL_CLA.
- MSI_CLP: a cloud property product derived from passive multispectral observations by MSI (Wang et al., 2023).
- AUX_3JH: an auxiliary product providing atmospheric and surface parameters (JAXA, 2026).

In terms of spatial resolution, the ATL_CLA and AC_CLP products are provided at a horizontal resolution of 1 km and a vertical resolution of 100 m, while the MSI_CLP product has a higher horizontal resolution of approximately 0.5 km. The vertical and horizontal resolutions of ATL_CLA and AC_CLP are consistent with each other.

https://doi.org/10.5194/egusphere-2026-4324
Preprint. Discussion started: 13 August 2026

Regarding data availability, the ATL_CLA, AC_CLP, and MSI_CLP products are publicly available and can be accessed through the JAXA G-Portal (https://gportal.jaxa.jp) as well as ESA Earth Online (https://earth.esa.int/eogateway/missions/earthcare). The AUX_3JH product is a non-public auxiliary product generated for ALL_RAD processing, whereas AUX_3D is provided as the corresponding public auxiliary product (JAXA, 2026). Both products are generated by interpolating meteorological fields from the ESA X-MET product (Eisinger et al., 2024) and provide atmospheric and surface parameters, including pressure, temperature, and water vapor profiles, as well as surface properties such as skin temperature, albedo, 10-m wind components, and sea ice cover. AUX_3JH further includes additional parameters required for ALL_RAD radiative transfer calculations, including surface emissivity required for longwave calculations. The surface emissivity is derived from the UW Baseline Fit Emissivity Database based on MODIS observations (Seemann et al., 2008) and the ASTER Global Emissivity Dataset (Hulley et al., 2015). Together, these input products provide complementary information on the vertical structure and microphysical properties of clouds and aerosols, as well as the thermodynamic and surface conditions required for radiative transfer calculations.

The ALL_RAD product evaluated in this study is version Ba, corresponding to the first public release on 1 December 2025. The versions of the input products used in this study are as follows: ATL_CLA version Cb, AC_CLP version Ca, MSI_CLP version Ca, and AUX_3JH version Ca. For comparison, the BMA-FLX product version Ba is used. Detailed information on the implementation status and known issues of each JAXA Level-2 product version is available from the JAXA EORC website (https://www.eorc.jaxa.jp/EARTHCARE).

2.2 Construction of composite cloud and aerosol profiles

In this subsection, we describe the construction of composite vertical profiles of clouds and aerosols used as input to the radiative transfer calculations. The ALL_RAD algorithm generates profiles only along the nadir track of EarthCARE, where observations from CPR, ATLID, and MSI are co-located. Off-nadir regions are not considered. The composite profiles are defined on a grid consistent with the CPR footprint, with a horizontal resolution of 1 km and a vertical resolution of 100 m. Variables from MSI_CLP, which have different spatial resolutions, are mapped onto this grid through selection or spatial averaging.

The cloud vertical profiles are constructed by combining retrievals from AC_CLP, ATL_CLA, and MSI_CLP. For most atmospheric conditions, vertical profiles of cloud liquid and ice water contents and effective radii are primarily taken from the AC_CLP product, which provides synergistic radar–lidar retrievals based on CPR and ATLID observations. Since CPR observations are limited to altitudes below approximately 20 km, the cloud profiles provided by AC_CLP are also generally restricted to below this altitude. In contrast, ATLID observations are available up to approximately 40 km. To represent high-altitude clouds such as polar stratospheric clouds (PSCs), cloud information above 20 km is also required. Therefore, to extend the cloud profiles into the upper atmosphere, cloud extinction coefficients from ATL_CLA are converted into cloud water content and used above 20 km.

https://doi.org/10.5194/egusphere-2026-4324
Preprint. Discussion started: 13 August 2026

The resulting cloud water content and effective radius profiles are then further adjusted using cloud optical thickness (COT) from MSI_CLP through a scaling procedure applied to the cloud water content, while keeping the effective radius unchanged. Although MSI_CLP also provides effective radius and cloud phase, these variables are not used in ALL_RAD version Ba. This COT-based scaling is introduced as a provisional treatment to incorporate passive sensor information into the composite cloud profiles. ACM_CLP, a combined product integrating CPR, ATLID, and MSI retrievals (ACM_CLP; Sato et al., 2025), has already been released and is available (Fig. 1); however, it is not used in ALL_RAD version Ba. In the future, the use of such a product is expected to provide more consistent cloud properties and eliminate the need for the COT-based scaling.

In contrast, aerosol vertical profiles used in the ALL_RAD algorithm are taken from the ATL_CLA product, which provides vertically resolved aerosol properties derived from ATLID measurements over a vertical range extending up to approximately 40 km altitude. Although aerosol products based on MSI observations are planned as part of the JAXA Level-2 suite, they are not yet available at the time of this study and are therefore not included in the current processing.

2.3 Radiative transfer calculation

In this subsection, we describe the radiative transfer calculations performed in the ALL_RAD algorithm. The composite cloud and aerosol profiles constructed in Section 2.2, defined on a grid with a horizontal resolution of 1 km and a vertical resolution of 100 m, are used as input to the one-dimensional radiative transfer model MstrnX (Nakajima et al., 2000; Sekiguchi and Nakajima, 2008), which calculates broadband radiative fluxes using a two-stream flux approximation. All radiative transfer calculations are performed on this grid. Using these input profiles, broadband shortwave and longwave radiative fluxes are calculated at the TOA, within the atmosphere, and at the surface, together with the corresponding radiative heating rate profiles.

In implementing the radiative transfer calculations, we take particular care to ensure consistency between the optical properties used in the radiative transfer model and those assumed in the Level-2 retrieval algorithms. For cloud properties, the scattering characteristics are selected to be consistent with the COT retrieval in MSI_CLP (Wang et al., 2023). Based on the cloud phase flag provided by MSI_CLP, Mie scattering is applied when the COT is retrieved under the assumption of liquid clouds, whereas for ice clouds, scattering properties based on non-spherical Voronoi ice particle models (Ishimoto et al., 2012; Letu et al., 2012, 2016) are used. Similarly, aerosol optical properties are defined consistently with the seven aerosol types used in ATL_CLA (Nishizawa et al., 2026), namely Smoke, Pollution, Marine, Pristine, Dust, Dusty mixture, and Unknown. The corresponding microphysical and optical parameters, including refractive indices and particle size distributions for coarse and fine modes, are assigned to each aerosol type.

To quantify the radiative effects of aerosols and clouds in a manner consistent with the definition of radiative forcing in Yamauchi et al. (2024), the algorithm computes radiative fluxes under four atmospheric conditions: all-sky, clear-sky (without clouds), cloudy-sky (without aerosols), and pristine-sky (without clouds and aerosols). The aerosol and cloud radiative forcing variables provided in the ALL_RAD product are defined as instantaneous values based on these flux calculations.

https://doi.org/10.5194/egusphere-2026-4324
Preprint. Discussion started: 13 August 2026

2.4 Output variables and specifications

In this subsection, we describe the main radiative output variables of the ALL_RAD algorithm and their specifications. The ALL_RAD product provides radiative quantities at two horizontal resolutions, depending on the application. The nominal spatial resolution of the ALL_RAD product is 10 km × 10 km, which defines the standard configuration of the radiation budget product and is consistent with the EarthCARE mission requirement to achieve an accuracy of approximately ±10 W m^{-2} in radiative flux estimates at a spatial scale of about 100 km^2 (Wehr et al., 2023). These 10 km values are obtained by averaging radiative fluxes and heating rate profiles calculated at a horizontal resolution of 1 km along the nadir track.

In addition, the ALL_RAD product provides radiative fluxes at a horizontal resolution of 1 km along the nadir track to enable flexible spatial aggregation for comparison with external reference products. In this study, the 1 km ALL_RAD fluxes are averaged over the along-track extent corresponding to the BMA-FLX assessment domain, which is defined for the EarthCARE radiative closure assessment as approximately 21 km along-track × 5 km across-track (Barker et al., 2025) and for which BMA-FLX provides flux estimates (Velázquez Blázquez et al., 2024b). This averaged nadir estimate is then compared with the BMA-FLX assessment-domain mean. At the 1 km resolution, only radiative fluxes are provided, while heating rate profiles are not included.

Table 1. Main radiative output variables and specifications of the ALL_RAD version Ba product. Panel (a) summarizes the standard output provided at a 10 km along-track resolution, and panel (b) summarizes the auxiliary output variables for radiative fluxes provided at a 1 km along-track resolution. The standard output includes radiative fluxes, aerosol radiative forcing, cloud radiative forcing, and radiative heating rates, whereas the auxiliary 1 km output is provided for flexible spatial aggregation and validation against external reference products. SW and LW denote shortwave and longwave radiation, respectively. For radiative fluxes and heating rates, the four conditions are defined as follows: all-sky includes both clouds and aerosols, clear-sky excludes clouds but includes aerosols, cloudy-sky includes clouds but excludes aerosols, and pristine-sky excludes both clouds and aerosols. For aerosol radiative forcing, "all" and "clear" denote conditions with and without clouds, respectively. For cloud radiative forcing, "polluted" and "clean" denote conditions with and without aerosols, respectively. The terms "aerosol radiative forcing" and "cloud radiative forcing" follow the product variable names and correspond to instantaneous aerosol and cloud radiative effects, respectively.

a) Standard output: 10 km along-track resolution

<table>
<tr><th>Variable</th><th>Horizontal</th><th>Vertical</th><th>Spectral component</th><th>Level</th><th>Direction</th><th>Condition</th></tr>
<tr><td>Radiative flux</td><td rowspan="3">10 km</td><td rowspan="3">-</td><td rowspan="4">SW / LW</td><td rowspan="3">TOA / Surface</td><td>Upward / Downward</td><td>all-sky, clear-sky, cloudy-sky, pristine-sky</td></tr>
<tr><td>Aerosol radiative forcing</td><td>-</td><td>all, clear</td></tr>
<tr><td>Cloud radiative forcing</td><td>-</td><td>polluted, clean</td></tr>
<tr><td>Radiative heating rate</td><td>10 km</td><td>500 m</td><td>-</td><td>-</td><td>all-sky, clear-sky, cloudy-sky, pristine-sky</td></tr>
</table>

b) Auxiliary output: 1 km along-track resolution

Variable	Horizontal	Vertical	Spectral component	Level	Direction	Condition
Radiative flux	1 km	-	SW / LW	TOA / Surface	Upward / Downward	all-sky, clear-sky, cloudy-sky, pristine-sky

https://doi.org/10.5194/egusphere-2026-4324
Preprint. Discussion started: 13 August 2026

Radiative fluxes are reported at the TOA and at the surface, whereas radiative heating rates are provided as vertical profiles within the atmosphere. These variables are provided for both shortwave (SW) and longwave (LW) components, for upward and downward directions, and under four atmospheric conditions (all-sky, clear-sky, cloudy-sky, and pristine-sky) as defined in Section 2.3.

Table 1 summarizes the main radiative output variables and their specifications. In this table, the terms “aerosol radiative forcing” and “cloud radiative forcing” follow the product variable names and correspond to instantaneous aerosol and cloud radiative effects, respectively.

3 Evaluation of TOA radiative fluxes against BMA-FLX

In this section, we evaluate the performance of the ALL_RAD product by comparing TOA radiative fluxes with those from the BMA-FLX product (Velázquez Blázquez et al., 2024b), which is derived from BBR observations. This comparison assesses the consistency of ALL_RAD TOA radiative flux estimates with an independent BBR-derived flux product.

BMA-FLX is an ESA Level-2 product that estimates instantaneous TOA SW and LW radiative fluxes from BBR broadband radiance measurements. The BBR observes each scene from three viewing directions (nadir, fore, and aft), and the filtered radiances are first converted into unfiltered broadband radiances by the ESA Level-2 BM-RAD product (Velázquez Blázquez et al., 2024a). In BMA-FLX, these radiances are converted into TOA fluxes using radiance-to-flux conversion algorithms based on angular distribution models (ADMs), with additional scene information from MSI and ATLID. The BMA-FLX product provides fluxes at both the standard resolution of 10 km × 10 km and the assessment domain resolution of approximately 21 km × 5 km, the latter of which is used in this study. In the following comparisons, the ALL_RAD estimates represent nadir-track averages over the along-track extent corresponding to the BMA-FLX assessment domain, whereas BMA-FLX represents the mean over the full assessment domain.

The evaluation is conducted at the instantaneous level using collocated observations from the two products. We first present a representative case to illustrate the consistency between ALL_RAD and BMA-FLX, followed by a comprehensive statistical comparison over all available scenes. The analysis further examines the spatial distribution of errors, their dependence on cloud regimes, and the effects of cloud cover and spatial representativeness differences between the two products.

3.1 Case study: example scene

To illustrate the consistency between ALL_RAD and BMA-FLX, we first present a representative scene (Figure 2). The MSI composite image (Fig. 2a) shows a heterogeneous cloud field along the EarthCARE track, including optically thick and thin cloud and clear regions. The TOA SW and LW radiative fluxes derived from ALL_RAD and BMA-FLX (Fig. 2b, c) are

https://doi.org/10.5194/egusphere-2026-4324
Preprint. Discussion started: 13 August 2026

generally in good agreement, capturing the spatial variability associated with the cloud structures. Differences between the two estimates are small compared to the overall magnitude of the fluxes. The vertical profiles of SW and LW radiative heating rates derived from ALL_RAD (Fig. 2d, e) exhibit physically consistent structures, with shortwave heating distributed throughout the atmosphere due to gaseous absorption and enhanced within cloud layers, while longwave cooling is distributed within and above the cloud layers. Overall, this example demonstrates that the ALL_RAD estimates are consistent with BMA-FLX while capturing the key radiative signatures associated with the cloud structures.

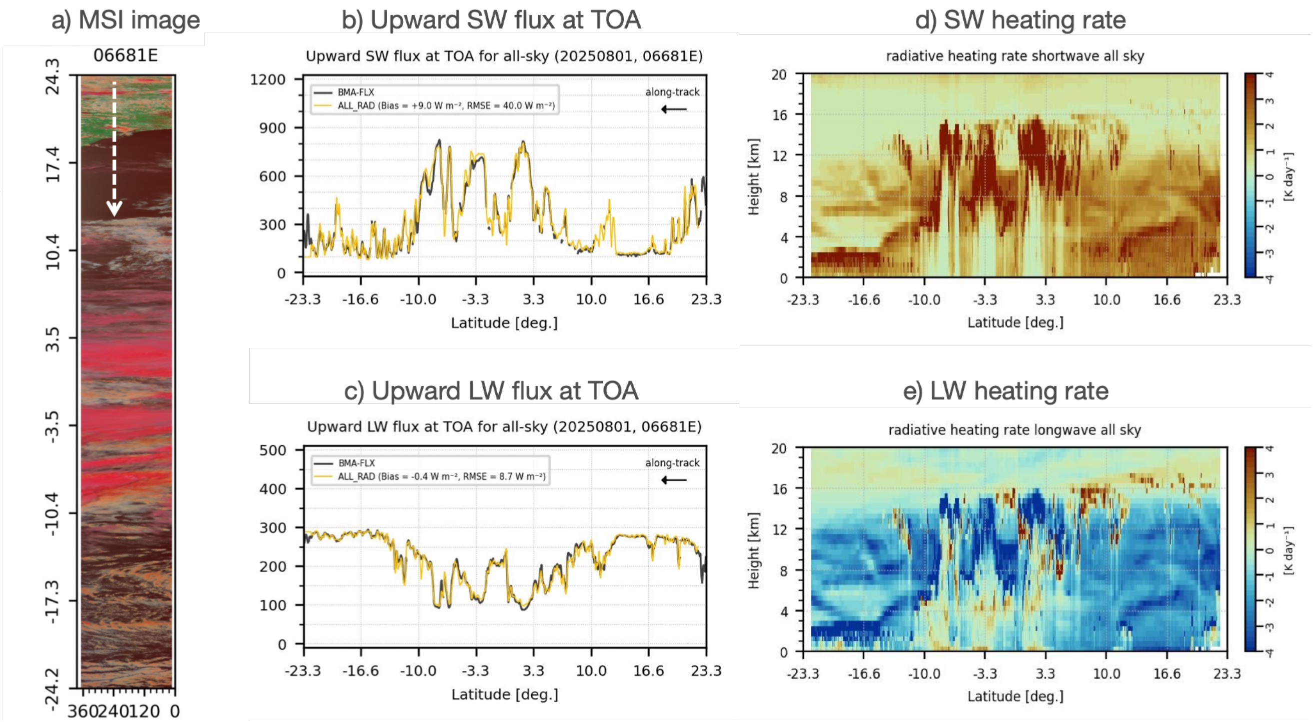

Figure 2. Example scene illustrating the comparison between ALL_RAD and BMA-FLX, observed on 1 August 2025 (frame ID: 06681E). (a) MSI composite image (RGB: bands 1, 3, and 4; 0.67, 1.65, and 2.21 µm) showing the cloud field along the EarthCARE track. (b) Shortwave (SW) and (c) longwave (LW) upward radiative fluxes at the top of the atmosphere (TOA) from ALL_RAD (yellow) and BMA-FLX (black). Vertical profiles of (d) SW and (e) LW radiative heating rates derived from ALL_RAD.

3.2 Global comparison of instantaneous TOA fluxes

To quantitatively assess the agreement between ALL_RAD and BMA-FLX, we compare instantaneous TOA radiative fluxes at the assessment domain resolution (21 km × 5 km). Figure 3 shows scatter plots of SW and LW TOA fluxes derived from ALL_RAD against those from BMA-FLX under all-sky conditions for all available scenes in August 2025. Overall, the TOA radiative fluxes from ALL_RAD are in close agreement with those from BMA-FLX. The SW comparison is based on daytime scenes only, whereas the LW comparison includes both daytime and nighttime scenes. The correlation coefficients

https://doi.org/10.5194/egusphere-2026-4324
Preprint. Discussion started: 13 August 2026

are high for both SW (r = 0.97) and LW (r = 0.99), indicating that the spatial variability of radiative fluxes is well captured by the ALL_RAD estimates.

For SW fluxes, the overall bias for the entire dataset is small (−0.6 W m⁻²), while the spread is relatively large (RMSE = 33.7 W m⁻²), reflecting the strong sensitivity of shortwave radiation to cloud properties and horizontal variability. It should be noted that, for large SW fluxes (around 800 W m⁻² in BMA-FLX), the ALL_RAD estimates exhibit a tendency to saturate. These points correspond to scenes with extremely high cloud optical thickness, typically associated with deep convective clouds. This behavior is consistent with the saturation of COT retrievals in MSI_CLP (COT = 150), which limits the variability captured in the ALL_RAD estimates.

In contrast, LW fluxes show both small bias (+2.2 W m⁻²) and significantly smaller spread (RMSE = 8.1 W m⁻²), indicating more stable agreement between the two products. These results demonstrate that ALL_RAD provides broadly consistent TOA radiative flux estimates at the instantaneous level, while capturing the variability associated with cloud–radiation interactions.

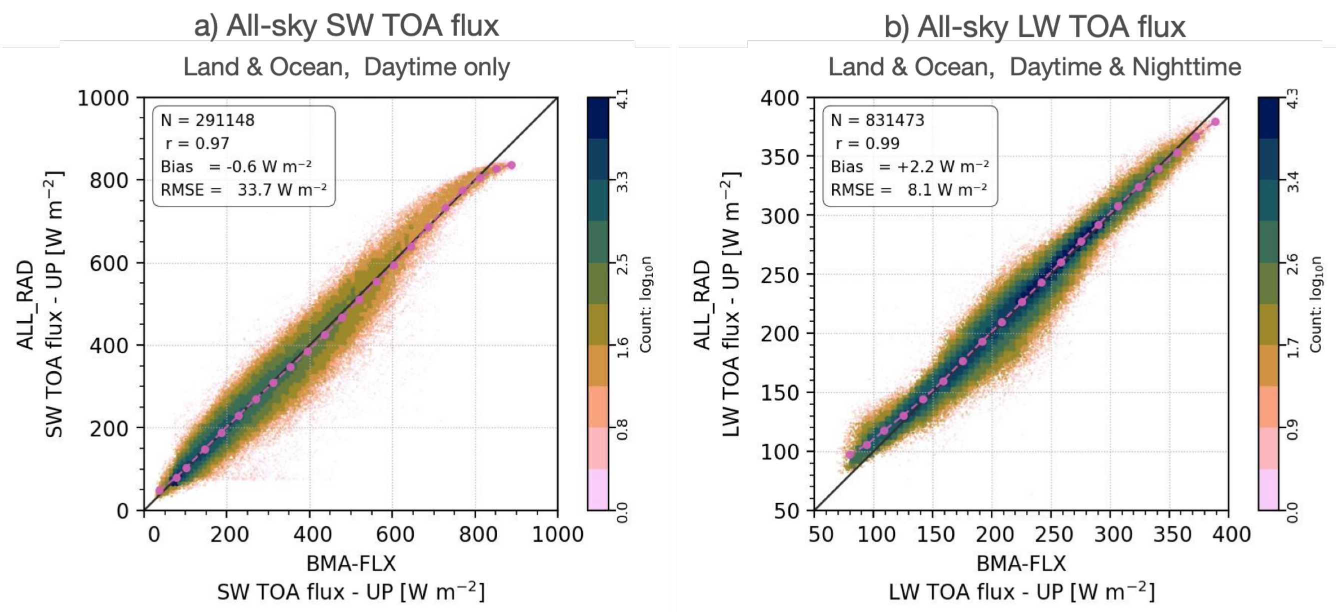

Figure 3. Scatter plots comparing instantaneous all-sky top-of-atmosphere (TOA) radiative fluxes from ALL_RAD and BMA-FLX at the assessment domain resolution (21 km along-track × 5 km across-track) for August 2025. Panels show (a) shortwave (SW) upward TOA fluxes for daytime scenes only and (b) longwave (LW) upward TOA fluxes for both daytime and nighttime scenes. The color shading indicates data density (logarithmic scale). Solid black lines denote the 1:1 relationship, and magenta dots represent binned averages. Statistical metrics, including the number of samples (N), correlation coefficient (r), bias, and root-mean-square error (RMSE), are shown in each panel. Color scales are adjusted separately for each panel.

https://doi.org/10.5194/egusphere-2026-4324
Preprint. Discussion started: 13 August 2026

3.3 Spatial distributions of bias and variability

To examine the geographical characteristics of the differences between ALL_RAD and BMA-FLX, Figure 4 shows the global distributions of bias and error standard deviation (SD) of ALL_RAD relative to BMA-FLX at the assessment domain resolution. For SW fluxes during daytime (Fig. 4a), the bias is generally small over most regions, with some regional structures associated with cloud regimes. In contrast, the error SD is relatively large (Fig. 4d), particularly in regions characterized by strong cloud variability, such as tropical convective areas and midlatitude storm tracks.

It should be noted that closer inspection of Figs. 4a and 4d reveals regions of negative bias and relatively large error SD over major high-altitude areas, including the Rocky Mountains, the Andes, and the Himalayas. These features are consistent with known issues in the MSI_CLP version Ca product, in which COT retrievals are not performed over high-elevation regions. As a result, the COT-based scaling described in Section 2.2 is not applied in these areas, leading to systematic differences in the SW flux estimates.

For LW fluxes during daytime, both the bias (Fig. 4b) and error SD (Fig. 4e) are smaller than those for SW, indicating more consistent agreement between ALL_RAD and BMA-FLX. The spatial variability of the errors is also reduced compared to SW. During nighttime, LW fluxes exhibit relatively uniform distributions of bias (Fig. 4c) and error SD (Fig. 4f), reflecting the absence of shortwave effects and the more homogeneous behavior of longwave radiation. Overall, the spatial patterns of error SD indicate that discrepancies between the two products are strongly linked to cloud variability, particularly for shortwave radiation, while LW fluxes show more stable agreement across different regions and conditions.

https://doi.org/10.5194/egusphere-2026-4324
Preprint. Discussion started: 13 August 2026

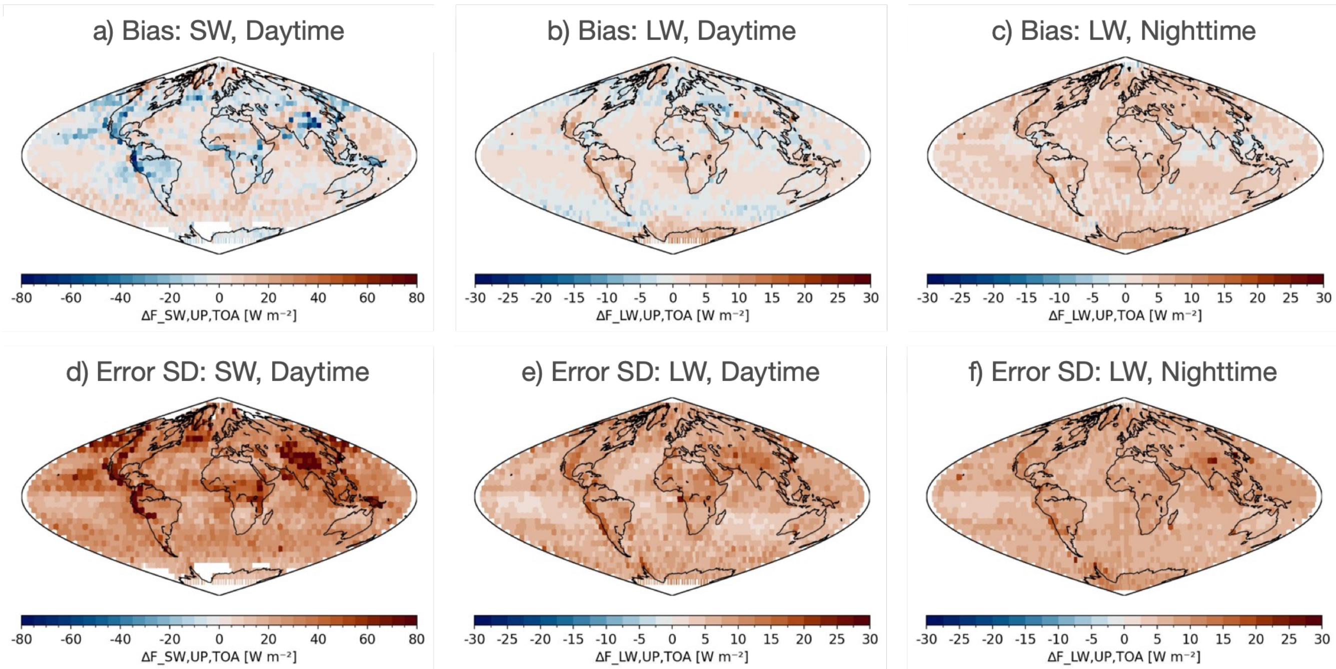

Figure 4. Global distributions of bias and error standard deviation (SD) of all-sky TOA radiative flux differences between ALL_RAD and BMA-FLX for August 2025. The statistics are computed from instantaneous differences at the assessment domain resolution (21 km along-track × 5 km across-track) and then averaged onto 5° × 5° latitude–longitude grids. The top row shows the bias, and the bottom row shows the error SD. Panels (a, d), (b, e), and (c, f) correspond to daytime SW, daytime LW, and nighttime LW fluxes, respectively. Positive bias indicates larger fluxes in ALL_RAD than in BMA-FLX.

3.4 Dependence of cloud regimes

To further investigate the sources of errors in the ALL_RAD estimates, we examine the relative contributions of bias and variability by analyzing their dependence on cloud regime. Since the RMSE can be decomposed as $RMSE^2 = bias^2 + SD^2$, this approach allows us to assess whether systematic or random components dominate the total error. As shown in Sections 3.2 and 3.3, the RMSE of LW fluxes is generally below 10 W m^{-2}, which is comparable to the EarthCARE mission requirement scale. Therefore, we focus here on SW fluxes to identify the dominant sources of error. The analysis is performed by classifying the data according to COT and cloud-top temperature (CTT).

Figure 5 shows the distributions of bias and SD as functions of COT and CTT over ocean during daytime. Here, it should be noted that not only COT but also CTT used in Fig. 5 are derived from MSI observations. Although cloud-top information from CPR and ATLID is generally expected to provide a more accurate representation of the physical cloud-top height, MSI-derived CTT is intentionally used here to characterize the error properties of ALL_RAD. This is because the MSI_CLP algorithm retrieves both COT and CTT consistently using cloud-phase classification based on thermal infrared brightness temperatures. Specifically, clouds with brightness temperatures in MSI band 6 (10.8 μm) higher than 265 K are retrieved using

https://doi.org/10.5194/egusphere-2026-4324
Preprint. Discussion started: 13 August 2026

the liquid-cloud assumption, whereas clouds with brightness temperatures lower than 265 K, including both mixed-phase and ice clouds, are retrieved using the ice-cloud assumption.

Figure 5a indicates that the SW flux bias varies systematically with cloud regime. In many regions of COT–CTT space, the magnitude of the bias exceeds the dataset-mean bias shown in Fig. 3a, and both positive and negative values are observed. This indicates that the small dataset-mean bias in Fig. 3a arises from compensation among regime-dependent biases of opposite signs.

Four characteristic groups corresponding to different cloud regimes can be identified. First, in the regions with COT < 4, positive biases are observed in most regions of the COT–CTT space, and this tendency is particularly pronounced for CTT < 225 K. Since the present analysis is not restricted to overcast clouds, these regions are likely to include not only optically thin clouds such as cirrus but also partially cloudy pixels containing clear-sky regions at the sub-pixel scale. In contrast, negative biases dominate in the regions with COT > 60 corresponding to optically very thick clouds. Furthermore, in the intermediate optical thickness range of 4 < COT < 60, different tendencies are observed depending on CTT. Specifically, negative biases dominate for CTT > 270 K, whereas positive bias tendencies are found for CTT < 270 K. These regimes are considered to correspond primarily to warm lower-level liquid-water clouds and colder mixed-phase/ice clouds, respectively.

The dependence of the error SD of SW fluxes on cloud regime is also examined (Fig. 5b). Although less pronounced than the bias patterns, the SD exhibits a similar regime dependence. The most prominent feature appears in the region corresponding to 4 < COT < 60 and CTT > 270 K, which mainly includes low-level liquid-water clouds. In this region, the error SD is approximately 10 W m^{-2} larger than in the surrounding regions. Comparison of Figs. 5a and 5b further shows that the amplitude of the error SD is larger than the corresponding bias in many regions. Considering the relationship $RMSE^2 = bias^2 + SD^2$, this suggests that the RMSE of the instantaneous SW fluxes shown in Fig. 3a is dominated primarily by the error SD rather than by systematic bias, with error SDs of approximately 20 W m^{-2} or larger contributing substantially to the RMSE.

The regime dependence of the bias and error SD for LW fluxes is also examined using Figs. 5c and 5d, respectively. Compared with SW fluxes, both quantities show substantially weaker dependence on the COT–CTT space. The LW flux bias generally remains within approximately ±3 W m^{-2} in regions with CTT > 225 K, which account for the majority of the data samples (Fig. 5c). In contrast, for cold clouds with CTT < 225 K, both negative and positive biases ranging from approximately −9 to +6 W m^{-2} are observed depending on COT. However, the fraction of data associated with these cold-cloud regimes is relatively small. As a result, the mean LW flux bias remains small without significant compensation between biases of opposite signs across different regimes.

Similarly, the error SD of LW fluxes (Fig. 5d) also exhibits relatively weak dependence on cloud regime, with most values remaining within approximately 4–10 W m^{-2}. The spatial variability of the error SD in the COT–CTT space is also considerably smaller than that for SW fluxes. In addition, comparison of Figs. 5c and 5d shows that the error SD is larger than the corresponding bias in many regions. However, both the LW bias and error SD are substantially smaller than those in the SW case. These results are consistent with the small RMSE of LW fluxes shown in Fig. 3b and indicate that LW radiative fluxes are less sensitive than SW fluxes to cloud-regime-dependent variability.

https://doi.org/10.5194/egusphere-2026-4324
Preprint. Discussion started: 13 August 2026

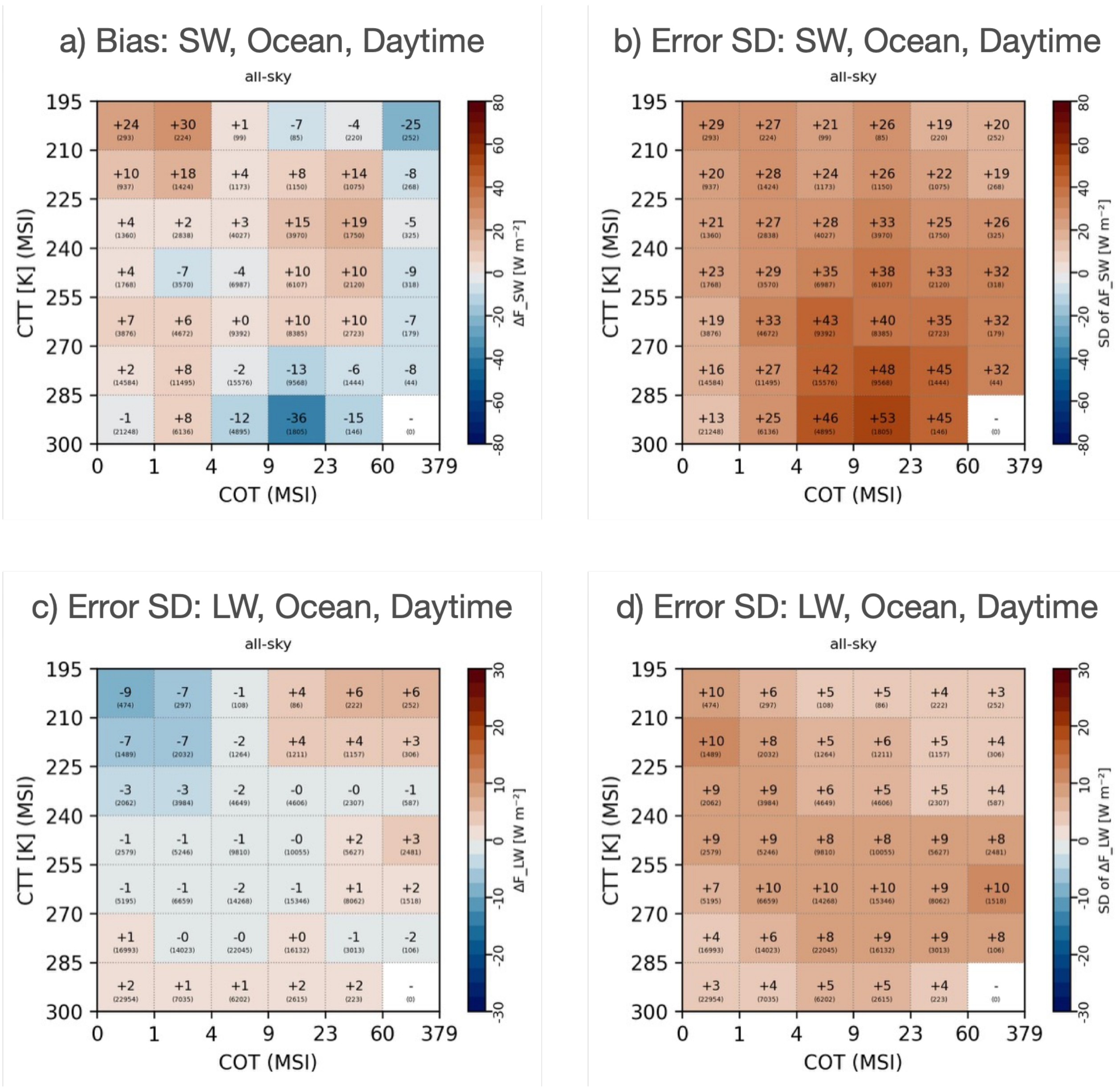

Figure 5. Dependence of bias and error standard deviation (SD) in all-sky TOA radiative flux differences between ALL_RAD and BMA-FLX on MSI-derived cloud optical thickness (COT) and cloud-top temperature (CTT) over ocean during daytime for August 2025. Panels show (a) bias and (b) error SD of shortwave (SW) fluxes, and (c) bias and (d) error SD of longwave (LW) fluxes. Values without parentheses indicate the bias or error SD, while values in parentheses indicate the number of samples in each bin. Positive bias indicates larger fluxes in ALL_RAD than in BMA-FLX.

https://doi.org/10.5194/egusphere-2026-4324
Preprint. Discussion started: 13 August 2026

3.5 Dependence on cloud cover and spatial representativeness

In this section, we investigate the relationship between SW flux errors and the horizontal cloud distribution within the BMA-FLX assessment domain. In the previous section, we showed that the bias and error SD of SW fluxes depend on cloud regime. In particular, the positive bias observed in low-COT regimes suggests a relationship with scenes containing partially cloudy conditions. In addition, since the RMSE of SW fluxes is predominantly influenced by the error SD, differences in spatial representativeness between the nadir-only observations of ALL_RAD and the assessment-domain-averaged BMA-FLX product may contribute to the errors. To investigate these effects, we first compare the COT–CTT distributions of bias and error SD for SW fluxes between partially cloudy and overcast conditions.

Figures 6a and 6b show the COT–CTT distributions of SW flux bias for partially cloudy (cloud cover = 10–90%) and overcast (cloud cover = 100%) conditions, respectively. The cloud fraction within the assessment domain is derived from the MSI-based cloud-cover variable ("cloud_cover") provided in the BMA-FLX product. For partially cloudy conditions (Fig. 6a), positive biases are found over almost the entire COT–CTT space. This positive bias may reflect multiple factors, including residual biases in clear-sky radiative properties, such as surface and aerosol characteristics, and possible biases in MSI-derived cloud properties caused by subpixel-scale cloud inhomogeneity. In contrast, for overcast conditions (Fig. 6b), both positive and negative bias regions coexist, exhibiting a more complex structure that depends on cloud regime. In particular, Fig. 6b shows a more pronounced negative bias tendency for low-level liquid-water stratocumulus clouds corresponding to $4 < \text{COT} < 60$ and $\text{CTT} < 270$ K.

Comparison of these bias patterns with Fig. 5a indicates that the positive bias found in the region with COT < 4 and CTT > 255 K in Fig. 5a is dominated primarily by partially cloudy cases. In contrast, the positive and negative bias patterns in the other regions mainly originate from overcast cases. These results indicate that the cloud-regime dependence of SW flux bias shown in Fig. 5a reflects a combination of systematic positive biases associated with partially cloudy conditions and more complex bias structures associated with overcast cloud regimes.

Similarly, the error SD of SW fluxes is also examined separately for partially cloudy and overcast conditions (Figs. 6c and 6d). The most notable feature is that the error SD is larger for overcast conditions than for partially cloudy conditions. In general, from the viewpoint of the representativeness of the BMA-FLX assessment domain by the nadir-only sampling of ALL_RAD, partially cloudy scenes are expected to be more strongly affected by spatial inhomogeneity, leading to larger error SDs. However, the results shown in Figs. 6c and 6d indicate that such a simple interpretation is insufficient.

These results indicate that the error SD of SW fluxes cannot be explained solely by differences in spatial representativeness but also by uncertainties in the cloud radiative field itself. In particular, for overcast scenes, differences in cloud optical properties and cloud vertical structures may strongly affect SW radiative fluxes, leading to larger discrepancies between ALL_RAD and BMA-FLX. In contrast, for partially cloudy scenes, the contribution of clear-sky regions within the assessment domain may relatively stabilize the spatially averaged SW fluxes.

https://doi.org/10.5194/egusphere-2026-4324
Preprint. Discussion started: 13 August 2026

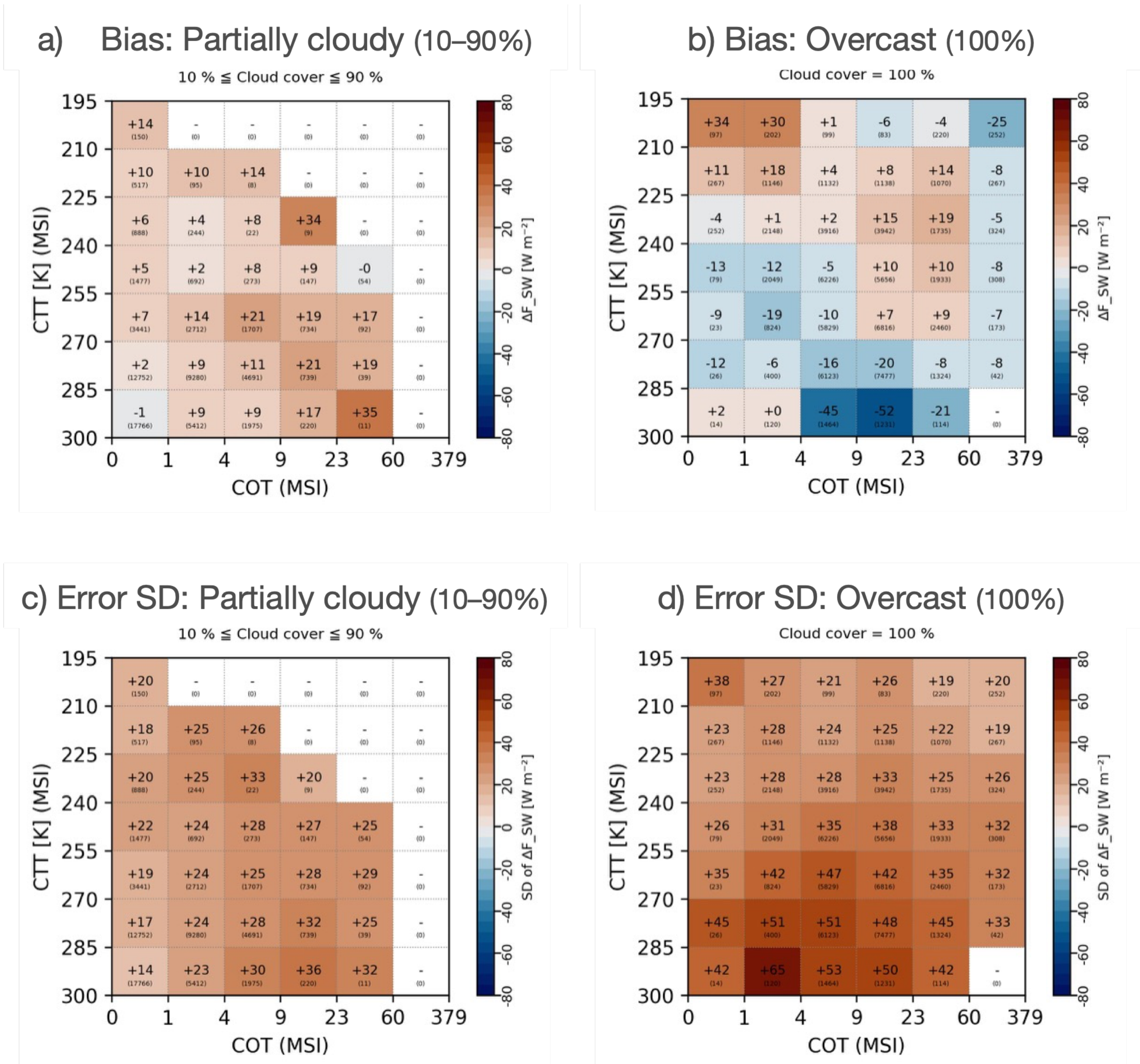

Figure 6. Dependence of bias and error standard deviation (SD) of all-sky shortwave (SW) TOA radiative flux differences between ALL_RAD and BMA-FLX on MSI-derived cloud optical thickness (COT) and cloud-top temperature (CTT) over ocean during daytime for August 2025, separated according to cloud cover within the BMA-FLX assessment domain. (a) Bias for partially cloudy conditions (cloud cover = 10–90%). (b) Bias for overcast conditions (cloud cover = 100%). (c) Error SD for partially cloudy conditions. (d) Error SD for overcast conditions. Values without parentheses indicate bias or error SD, while values in parentheses indicate the number of samples in each bin. Positive bias indicates larger fluxes in ALL_RAD than in BMA-FLX.

https://doi.org/10.5194/egusphere-2026-4324
Preprint. Discussion started: 13 August 2026

3.6 Summary of all-sky evaluation with BMA-FLX

Overall, the validation results demonstrate that ALL_RAD provides TOA radiative flux estimates that are generally consistent with the independent BMA-FLX product. In particular, LW fluxes exhibit small bias and error SD with relatively weak dependence on cloud regime, indicating stable performance across a wide range of cloud conditions. In contrast, SW fluxes show significant cloud-regime dependence, including systematic bias structures and relatively large error SDs associated with specific cloud regimes.

The analyses in Sections. 3.4 and 3.5 indicate that the RMSE of instantaneous SW fluxes is dominated primarily by scene-dependent variability rather than by systematic bias. The results further suggest that the SW flux differences cannot be explained solely by differences in spatial representativeness between the two products but also by uncertainties in cloud-radiative representation, particularly for overcast low-level liquid-water clouds. The remaining SW scatter may therefore reflect both limitations in the ALL_RAD cloud-radiative representation and uncertainties inherent in the comparison with BMA-FLX. Although non-negligible scatter remains at the individual scene level, the overall mean biases are relatively small. These results indicate that ALL_RAD is suitable for characterizing the mean radiative properties of clouds and the atmosphere.

4 Evaluation against BMA-FLX under cloud-free conditions

Although cloud-free pixels are included in the all-sky comparison in Section 3, we separately evaluate the ALL_RAD clear-sky fluxes by comparing them with BMA-FLX fluxes for cloud-free pixels. As described in Section 2.3, the ALL_RAD algorithm computes radiative fluxes for four atmospheric conditions: all-sky, clear-sky without clouds, cloudy-sky without aerosols, and pristine-sky without both clouds and aerosols. These flux estimates are then used to assess the radiative effects of clouds and aerosols. Since BMA-FLX provides observed/retrieved all-sky fluxes but not clear-sky fluxes, this evaluation is performed using cloud-free pixels, for which all-sky fluxes are expected to be equivalent to clear-sky fluxes. Because cloud radiative effects are derived from the difference between all-sky and clear-sky fluxes, assessing clear-sky flux accuracy is also an important part of the ALL_RAD evaluation.

Figure 7 compares TOA radiative fluxes from ALL_RAD and BMA-FLX for cloud-free pixels at the assessment domain resolution. Cloud-free pixels are selected using two criteria: cloud cover of 0% in the BMA-FLX assessment domain and no cloud layers detected by ATL_CLA.

Clear-sky SW fluxes show small mean biases of +3.0 W m^{-2} over ocean and −2.2 W m^{-2} over land (Figs. 7a and 7b). The corresponding RMSEs are 7.7 W m^{-2} and 13.5 W m^{-2}, respectively, which are substantially smaller than those found under all-sky conditions (Fig. 7a). This is reasonable because, except for snow- and ice-covered surfaces, both ocean and land surfaces are much darker than clouds in the shortwave spectral region. The error characteristics, however, differ between ocean and land. Over ocean, ALL_RAD shows a systematic positive difference relative to BMA-FLX. Given the relatively small variability of ocean surface albedo, this positive bias may be related to uncertainties in aerosol representation. Over land, in

https://doi.org/10.5194/egusphere-2026-4324
Preprint. Discussion started: 13 August 2026

contrast, both positive and negative differences are observed, suggesting that uncertainties in land surface albedo contribute to the scatter in clear-sky SW fluxes.

Clear-sky LW fluxes show good agreement over both ocean and land (Figs. 7c and 7d). The biases are small, +1.6 W m^{-2} over ocean and +2.1 W m^{-2} over land, and the corresponding RMSEs are 4.7 and 6.9 W m^{-2}, respectively. The plots include both daytime and nighttime scenes, forming two distinct clusters with higher and lower fluxes, respectively. The lower-flux cluster is mainly composed of scenes over the Antarctic continent and the surrounding Southern Ocean. A slight positive bias is observed in the lower-flux cluster, suggesting that clear-sky LW fluxes in cold nighttime polar regions may require further attention, which may reflect uncertainty in the surface temperature used as input. Apart from this feature, the overall agreement indicates that, in the absence of clouds, uncertainties related to temperature profiles, water vapor absorption, surface temperature, and surface emissivity have only a limited impact on the estimated LW TOA fluxes.

Overall, these clear-sky comparisons support the reliability of ALL_RAD clear-sky TOA flux estimates, while suggesting that residual uncertainties associated with aerosol representation and region-dependent surface properties may remain under some conditions. Together with the all-sky evaluation in Section 3, these results provide an important basis for evaluating cloud radiative effects derived from differences between all-sky and clear-sky fluxes. They also indicate that a more direct evaluation of aerosol radiative effects will require additional observations that simultaneously constrain aerosol optical properties and radiative fluxes.

https://doi.org/10.5194/egusphere-2026-4324
Preprint. Discussion started: 13 August 2026

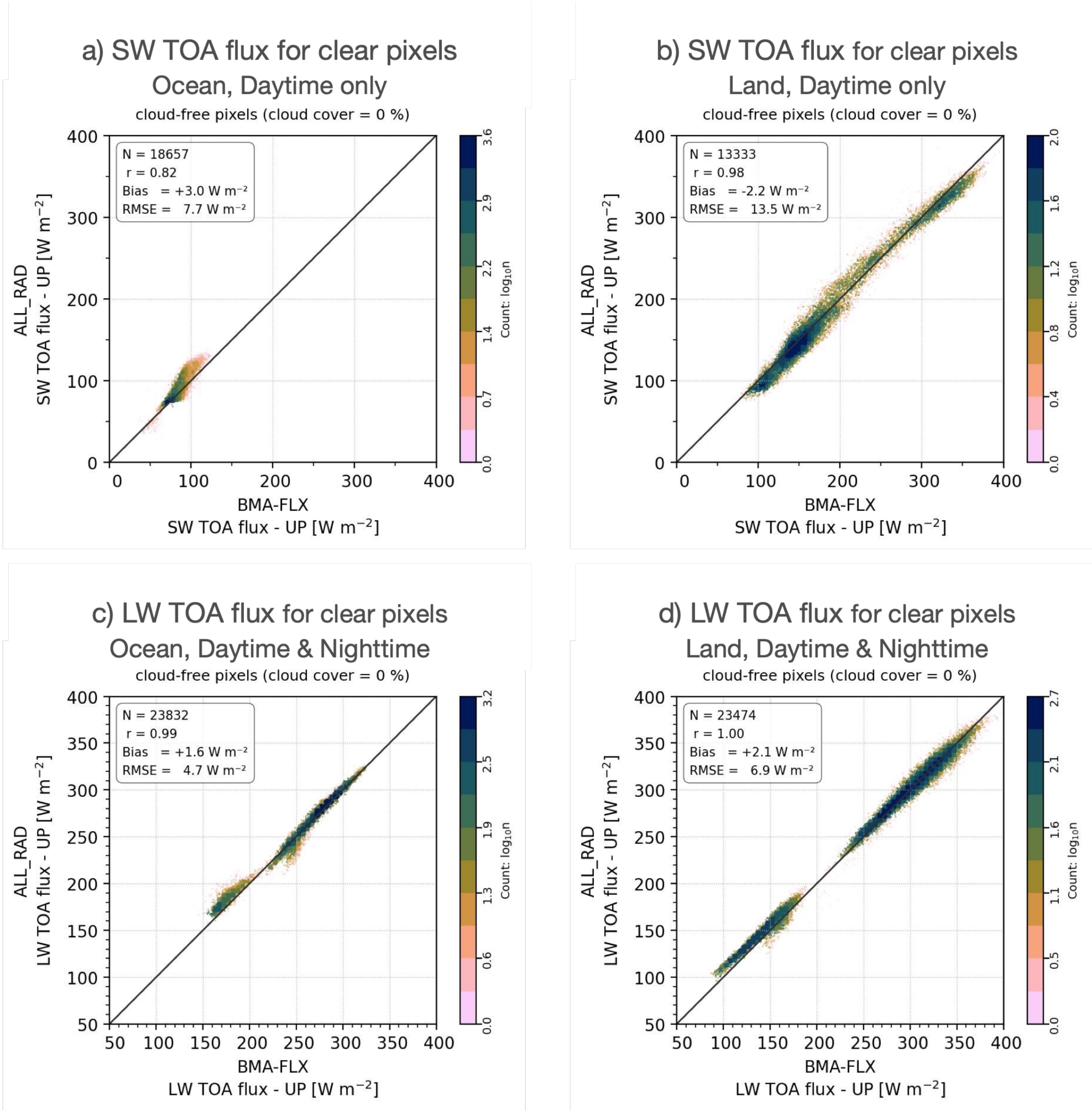

Figure 7. Scatter plots comparing top-of-atmosphere (TOA) radiative fluxes from ALL_RAD and BMA-FLX for cloud-free pixels at the assessment domain resolution (21 km along-track × 5 km across-track) for August 2025. Panels show shortwave (SW) fluxes (a) over ocean and (b) land for daytime samples, and longwave (LW) fluxes (c) over ocean and (d) land for both daytime and nighttime samples. The color shading indicates data density on a logarithmic scale, and the solid black lines denote the 1:1 relationship. Statistical metrics, including the number of samples (N), correlation coefficient (r), bias, and root-mean-square error (RMSE), are shown in each panel. Color scales are adjusted separately for each panel.

https://doi.org/10.5194/egusphere-2026-4324
Preprint. Discussion started: 13 August 2026

5 Evaluation of surface radiative fluxes against BSRN measurements

Following the TOA flux evaluation in Sections 3 and 4, we further evaluate the surface radiative flux estimates from ALL_RAD using ground-based observations. Evaluating surface fluxes in addition to TOA fluxes contributes to a broader assessment of radiative closure. Because the available matchups with ground-based observations are limited, the present analysis should be regarded as an initial assessment of the surface flux performance.

Surface downward SW and LW fluxes from ALL_RAD are compared with ground-based observations from the Baseline Surface Radiation Network (BSRN； Ohmura et al., 1998). The matchup is performed for BSRN sites located within 20 km of the EarthCARE ground track and within 10 min of the closest satellite overpass to each site. For each matchup, the ALL_RAD value is calculated as the spatial average of 1 km flux estimates within 20 km along the EarthCARE ground track from the BSRN site, whereas the corresponding BSRN value is calculated as the temporal average of observations within ±10 min of the overpass. These spatial and temporal criteria are chosen empirically to ensure a sufficient number of matchup samples while limiting representativeness differences between the satellite and ground-based observations. The comparison period extends from 3 April to 19 November 2025. During this period, five BSRN sites satisfy these matchup criteria: Abashiri, Japan; Cabauw, the Netherlands; Ny-Ålesund, Norway; Sonnblick, Austria; and Syowa Station, Antarctica. For each matchup, the horizontal and vertical error bars indicate the temporal variability of the BSRN observations and the spatial variability of the ALL_RAD estimates within the matchup window, respectively.

Figure 8a shows the comparison of downward SW surface fluxes. Although the number of matchups is limited, ALL_RAD captures the overall variability of the BSRN observations across a wide range of observed fluxes, as indicated by the high correlation coefficient of 0.94. The mean bias is small, -2.6 W m^{-2}, while the RMSE is 90.6 W m^{-2}. The relatively large scatter in some cases is not unexpected, because surface SW radiation is strongly affected by cloud variability, solar illumination conditions, and spatial representativeness differences between the satellite footprint and the point-scale ground observations.

Figure 8b shows the corresponding comparison for downward LW surface fluxes. The agreement is also good, with a correlation coefficient of 0.94, a very small mean bias of −0.2 W m^{-2} and an RMSE of 20.8 W m^{-2}. However, the RMSEs for the surface SW and LW fluxes are approximately three times larger than the corresponding TOA values shown in Fig. 3. This likely reflects the greater sensitivity of surface validation to spatial representativeness, especially under the relatively broad matchup criteria used in this study. Understanding these differences in more detail would require case-by-case examination of the cloud scenes and the associated matchup conditions. As the EarthCARE observation period continues and a larger number of matchups become available, more stringent matchup criteria and more robust surface flux validation will become possible.

Overall, these results indicate that ALL_RAD provides physically reasonable estimates of surface radiative fluxes in this initial comparison.

https://doi.org/10.5194/egusphere-2026-4324
Preprint. Discussion started: 13 August 2026

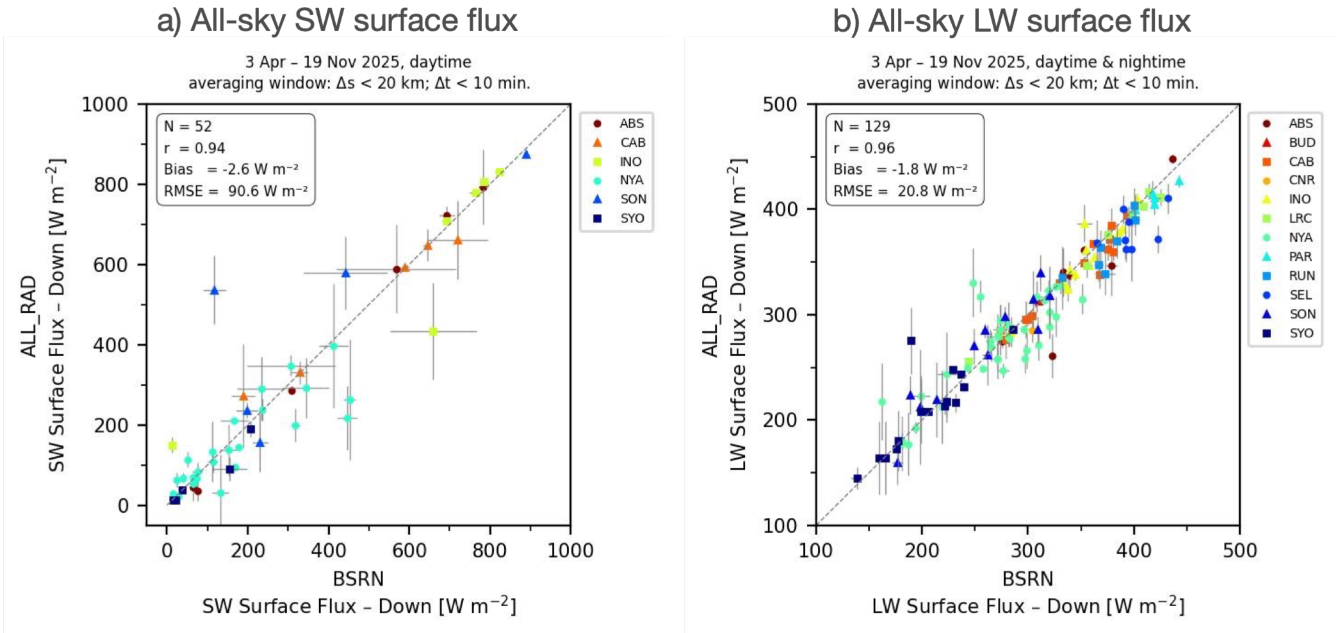

Figure 8. Comparison of all-sky downward surface radiative fluxes from ALL_RAD with ground-based observations from the Baseline Surface Radiation Network (BSRN). (a) Downward shortwave (SW) surface fluxes and (b) downward longwave (LW) surface fluxes. Matchups are selected for BSRN sites located within 20 km of the EarthCARE ground track and within 10 min of the closest satellite overpass to each site during the period from 3 April to 19 November 2025. Plotted points represent the spatial mean of ALL_RAD estimates within the 20 km along-track matchup window and the temporal mean of BSRN observations within ±10 min. Colors indicate different BSRN sites: ABS, Abashiri, Japan; BUD, Budapest-Lorinc, Hungary; CAB, Cabauw, the Netherlands; CNR, Cener, Spain; INO, Magurele, Romania; LRC, Langley Research Center, USA; NYA, Ny-Ålesund, Norway; PAR, Paramaribo, Surinam; RUN, Reunion Island; SEL, Selegua, Mexico; SON, Sonnblick, Austria; and SYO, Syowa Station, Antarctica. The dashed line denotes the 1:1 relationship. Error bars indicate the variability within the matchup window. Statistical metrics, including the number of samples, correlation coefficient, and bias, are shown in each panel.

6. Discussion

6.1 Demonstration of cloud radiative effects and heating rates

In Sections 3–5, the ALL_RAD radiative flux estimates were evaluated through comparisons with BMA-FLX and ground-based observations. These results provide a basis for using ALL_RAD in subsequent analyses and can be regarded as an initial step toward radiative closure assessment. In this subsection, we focus on two key quantities included in the ALL_RAD product, as listed in Table 1: the cloud radiative effect (CRE) and radiative heating rate (HR). We examine whether these quantities exhibit physically consistent features and are qualitatively consistent with previous studies.

Figure 9 shows the zonal-mean CREs for the SW, LW, and net (NET) components derived from ALL_RAD for August 2025. The CRE is defined for each spectral component and boundary level as the difference between all-sky and clear-sky net radiative fluxes:

https://doi.org/10.5194/egusphere-2026-4324
Preprint. Discussion started: 13 August 2026

$$CRE_{b,z} = \left(F_{b,z}{}^{\downarrow} - F_{b,z}{}^{\uparrow}\right)_{all-sky} - \left(F_{b,z}{}^{\downarrow} - F_{b,z}^{\uparrow}\right)_{clear-sky},$$

where b denotes the spectral component (SW, LW, or NET), z denotes the boundary level (TOA or BOA), and downward flux is taken as positive. The all-sky fluxes are calculated with clouds and aerosols, whereas the clear-sky fluxes are calculated without clouds but with aerosols. The atmospheric CRE (ATM CRE), representing the cloud radiative effect within the atmospheric column, is calculated as the difference between the TOA and BOA CREs:

$$CRE_{b,ATM} = CRE_{b,TOA} - CRE_{b,BOA}.$$

The radiative fluxes and CREs provided in the ALL_RAD product are instantaneous values at the EarthCARE observation time. In Fig. 9, the SW CRE values are scaled by the daily-mean solar irradiance to represent daily-mean values, and the NET CRE is calculated using this scaled SW component. This scaling accounts for the diurnal variation in incoming solar radiation, but the underlying cloud distributions remain tied to the EarthCARE observation time.

For the TOA CRE (Fig. 9a), corresponding estimates derived using BMA-FLX are also shown as dashed lines for comparison. Because BMA-FLX provides all-sky fluxes but not clear-sky fluxes, the ALL_RAD clear-sky fluxes are used as the clear-sky component when deriving CREs based on BMA-FLX. The same SW scaling is applied to the BMA-FLX-based TOA CREs. Thus, differences between the dashed and solid TOA CRE curves reflect differences in the all-sky TOA fluxes between the two products.

The TOA CREs derived from ALL_RAD agree well with those derived using BMA-FLX for the SW, LW, and NET components. This is consistent with the small mean differences between their TOA fluxes shown in Section 3. At both TOA and BOA (Fig. 9a and 9b), the SW CRE is negative. At TOA, this results from increased reflection of solar radiation back to space by clouds, whereas at BOA it results from reduced solar radiation reaching the surface. In contrast, the LW CRE is positive, representing the greenhouse effect of clouds. In most latitudes, the NET CRE is negative at both TOA and BOA because the negative SW contribution exceeds the positive LW contribution. The latitudinal variations in CRE amplitude are consistent with the expected influence of cloud amount and optical thickness on SW CRE, and cloud-top height on LW CRE.

The sign of the ATM CRE (Fig. 9c) varies with latitude. The SW ATM CRE is small but positive, consistent with shortwave absorption by clouds within the atmosphere. In contrast, the LW ATM CRE has a larger amplitude and changes sign from positive values in the tropics to negative values at higher latitudes. Consequently, the latitudinal structure of the NET ATM CRE is mainly determined by the LW component.

These latitudinal structures are qualitatively consistent with the characteristics of cloud radiative effects derived from CloudSat radiative flux products (e.g., L'Ecuyer et al., 2008). However, the present analysis is based only on one month of data, and longer-term analyses are needed to examine seasonal variations and climatological features.

https://doi.org/10.5194/egusphere-2026-4324
Preprint. Discussion started: 13 August 2026

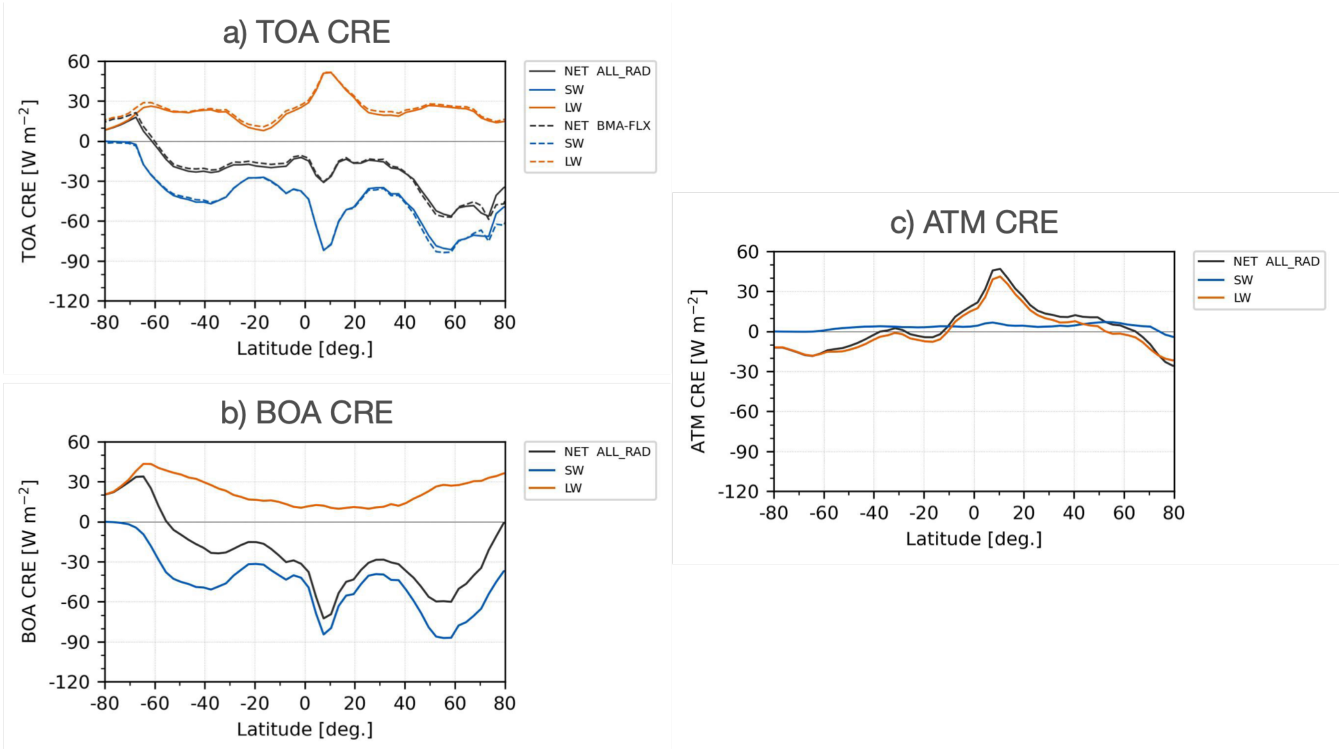

Figure 9. Zonal-mean cloud radiative effects (CREs) derived from ALL_RAD for August 2025. CRE is defined as the difference between all-sky and clear-sky net radiative fluxes. The SW CRE values are scaled by the daily-mean solar irradiance to represent daily-mean values. Panels show CREs (a) at the top of the atmosphere (TOA), (b) at the bottom of the atmosphere (BOA), and (c) within the atmosphere (ATM). The ATM CRE is calculated as the difference between TOA and BOA CREs. Shortwave (SW), longwave (LW), and net (NET) components are shown separately. Solid lines indicate ALL_RAD-derived CREs. For comparison, BMA-FLX-based TOA CREs, derived using BMA-FLX all-sky fluxes and ALL_RAD clear-sky fluxes, are shown with dashed lines.

We next examine the vertical structure of atmospheric HRs associated with CREs (Figure 10). The CRE HR, Q_{CRE}, is defined as the difference between the HRs under all-sky and clear-sky conditions, $Q_{all-sky}$ and $Q_{clear-sky}$, respectively:

$$Q_{b,CRE} = Q_{b,all-sky} - Q_{b,clear-sky}.$$

For consistency with the CRE analysis in Fig. 9, the SW CRE HRs in Fig. 10 are scaled by the daily-mean solar irradiance to represent daily-mean heating rates, and the NET CRE HR is calculated using this scaled SW component. This quantity provides a vertical decomposition of the ATM CRE shown in Fig.9, indicating how the cloud-induced radiative heating or cooling of the atmospheric column is distributed with height. The SW CRE HR is generally positive (Fig. 10a), consistent with the positive SW ATM CRE in Fig. 9c and with shortwave absorption by clouds. In contrast, the LW CRE HR exhibits a more

https://doi.org/10.5194/egusphere-2026-4324
Preprint. Discussion started: 13 August 2026

complex vertical structure (Fig. 10b), with positive values in the tropical middle-to-upper troposphere and negative values above these regions and at higher latitudes. The NET CRE HR (Fig. 10c) is therefore characterized by positive heating in the tropical middle-to-upper troposphere and cooling in the lower troposphere and at higher latitudes, consistent with the latitudinal structure of the NET ATM CRE shown in Fig. 9c.

These latitude–height structures of CRE HRs are qualitatively consistent with previous studies of cloud radiative heating based on A-Train observations (e.g., Kato et al., 2018). However, as with the CRE analysis, the present results are based only on one month of data, and the vertical heating-rate structures reflect cloud distributions sampled at the EarthCARE observation time. Longer-term analyses are therefore needed to examine seasonal variations and climatological features, and to place these EarthCARE-derived estimates in the context of knowledge accumulated from previous A-Train observations.

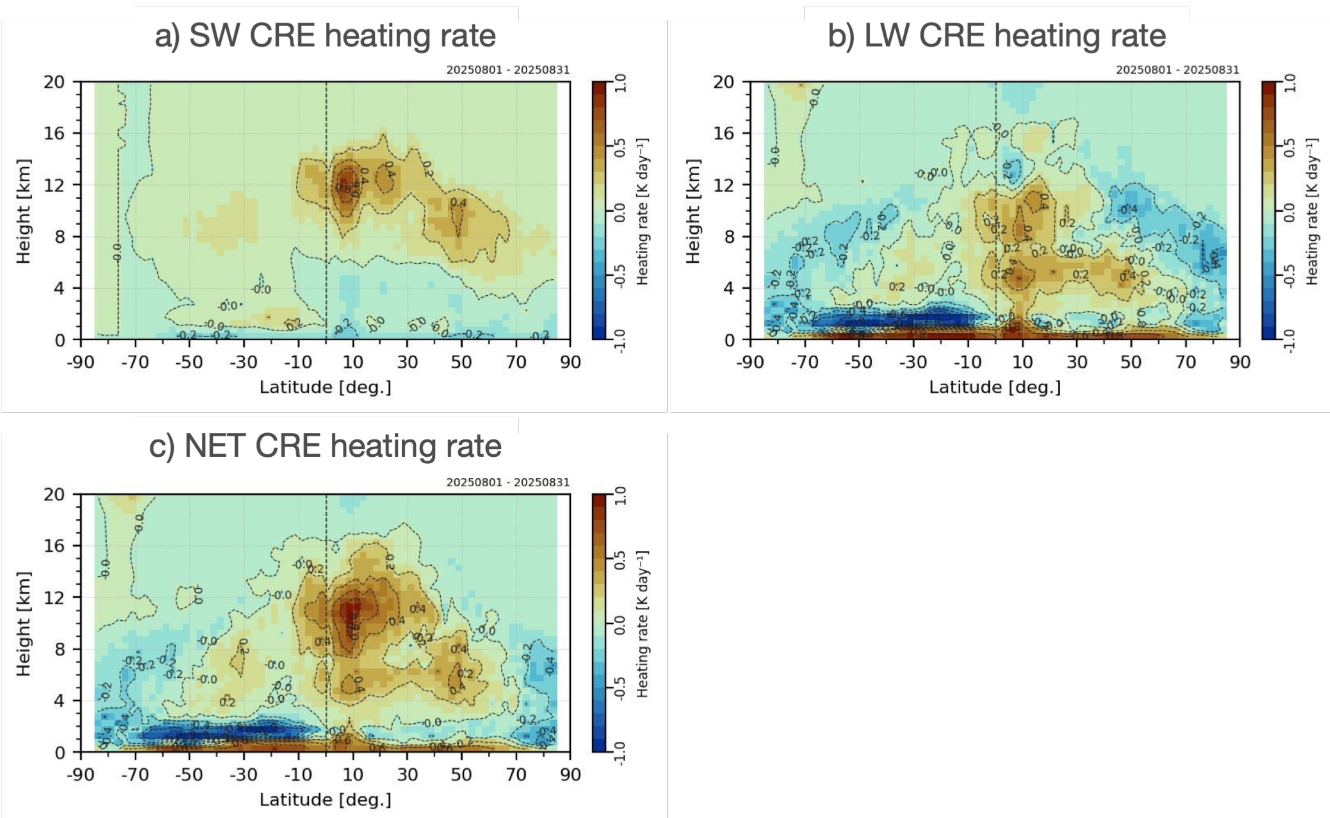

Figure 10. Latitude–height cross sections of cloud radiative effect heating rates (CRE HRs) derived from ALL_RAD for August 2025. The CRE HR is defined as the difference between all-sky and clear-sky radiative heating rates and represents the cloud-induced change in atmospheric radiative heating. The SW CRE heating rates are scaled by the daily-mean solar irradiance to represent daily-mean heating rates. Panels show the (a) shortwave (SW), (b) longwave (LW), and (c) net (NET) components. Positive values indicate cloud-induced radiative heating relative to clear-sky conditions, whereas negative values indicate cloud-induced radiative cooling.

https://doi.org/10.5194/egusphere-2026-4324
Preprint. Discussion started: 13 August 2026

6.2 Demonstration of aerosol radiative effects

As another initial demonstration, we present the global distribution of aerosol radiative effects (AREs) derived from ALL_RAD. This analysis illustrates the capability of ALL_RAD to diagnose AREs in a vertically consistent framework. Figure 11 shows the SW, LW, and NET AREs at the TOA, within the atmosphere (ATM), and at the BOA for daytime scenes in August 2025 under all-sky conditions. Although the analysis is limited to daytime scenes, this is not expected to compromise the purpose of providing an initial demonstration of ARE diagnostics, because the SW component is the primary contributor to the NET ARE. Note that the ALL_RAD product also provides AREs under clear-sky conditions as listed in Table 1.

The SW ARE is predominantly negative at the TOA and BOA, consistent with aerosol-induced scattering and absorption that increase reflected solar radiation and reduce the solar radiation reaching the surface. In contrast, the ATM SW ARE is positive, indicating shortwave absorption by aerosols within the atmosphere. These features are most pronounced over major aerosol source regions, including the Sahara Desert and biomass-burning regions in central and southern Africa, as well as their downwind regions.

The LW ARE exhibits a different vertical structure from the SW ARE. Positive LW AREs are found at the TOA and BOA, whereas the ATM LW ARE is negative in the global mean. Although the magnitude of the LW ARE is smaller than that of the SW ARE, it partly offsets the SW contribution to the net radiative effect.

Consequently, the NET ARE is largely controlled by the SW component. The global-mean NET AREs for the period analyzed here (August 2025) are estimated to be −1.5 W m^{-2} at the TOA, +1.2 W m^{-2} within the atmosphere, and −2.7 W m^{-2} at the BOA. Because the present ARE estimates are based on one month of data in August 2025, they should not be directly compared quantitatively with previous multi-year estimates based on A-Train observations. Nevertheless, the global patterns, signs, and vertical partitioning of the AREs among the TOA, ATM, and BOA are broadly consistent with the general characteristics reported in previous A-Train-based studies of aerosol radiative effects (Oikawa et al., 2013, 2018; Matus et al., 2019). Despite this qualitative consistency, validation of the radiative fluxes directly related to AREs remains limited in this study. In particular, the validity of the input aerosol types and optical properties, as well as the uncertainties in the radiative transfer calculations based on these inputs, have not been fully assessed. Therefore, the results shown here should be interpreted as an initial demonstration of ARE diagnostics based on the current version of ALL_RAD.

https://doi.org/10.5194/egusphere-2026-4324
Preprint. Discussion started: 13 August 2026

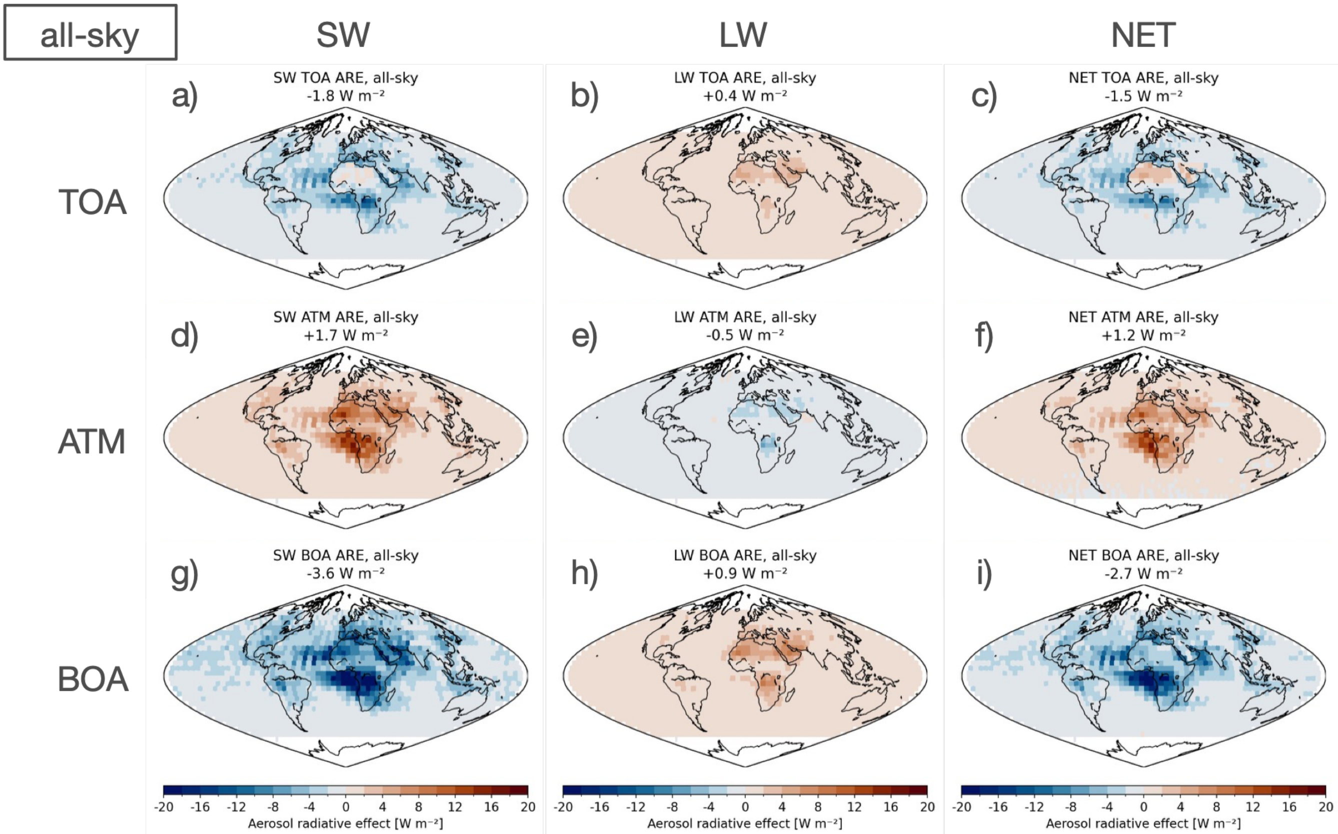

Figure 11. Global distributions of aerosol radiative effects (AREs) derived from ALL_RAD for daytime scenes in August 2025 under all-sky conditions. ARE is defined as the difference between aerosol-containing and aerosol-free radiative fluxes under the same all-sky conditions. The SW ARE values are scaled by the daily-mean solar irradiance to represent daily-mean values. Panels show AREs at the top of the atmosphere (TOA; a–c), within the atmosphere (ATM; d–f), and at the bottom of the atmosphere (BOA; g–i). Shortwave (SW; a, d, g), longwave (LW; b, e, h), and net (NET; c, f, i) components are shown separately. The ATM ARE is calculated as the difference between TOA and BOA AREs. Values shown below the panel titles indicate global means.

6.3 Sources of uncertainty and future perspectives

The results in Sections 3–5 support the basic reliability of the radiative fluxes and derived quantities provided by ALL_RAD. At the same time, systematic uncertainties related to cloud regime and cloud cover were identified, particularly for SW fluxes. In this section, we summarize the current status of ALL_RAD and discuss remaining issues for future improvement and validation.

This study provides an initial evaluation of ALL_RAD based on actual EarthCARE observations. The TOA radiative fluxes from ALL_RAD generally agree well with BMA-FLX (Fig. 3), and the surface radiative fluxes are also broadly consistent with BSRN observations, although the number of available matchups is limited (Fig. 8). These results represent an important step from the pre-launch evaluation by Yamauchi et al. (2024) toward evaluation based on actual EarthCARE observations.

https://doi.org/10.5194/egusphere-2026-4324
Preprint. Discussion started: 13 August 2026

This progress should be attributed not only to improvements in the ALL_RAD algorithm itself, but also to improvements in the input Level-2 cloud and aerosol products and advances in the calibration accuracy of the upstream Level-1 products.

In contrast to the LW fluxes, non-negligible uncertainties remain in the SW fluxes. The bias and error SD of the SW fluxes exhibit clear geographical patterns (Fig. 4) and depend on the COT–CTT space (Fig. 5) and cloud cover within the assessment domain (Fig. 6), with systematic features appearing in specific cloud regimes, such as low-level liquid-water clouds. These uncertainties may originate from multiple processing stages. Possible sources include cloud properties retrieved in the input AC_CLP and MSI_CLP products, the construction of combined cloud profiles in which AC_CLP-derived vertical cloud water contents are scaled using MSI-derived COT, and inconsistencies in the treatment of cloud particle scattering properties between the Level-2 retrieval algorithms and the ALL_RAD radiative transfer calculations. In addition, the positive bias tendency under partially cloudy conditions (Fig. 6a) may be related to clear-sky contamination at the subpixel scale, heterogeneity in cloud properties, or three-dimensional radiative effects, which could affect both the retrievals and the radiative flux calculations.

However, the ALL_RAD–BMA-FLX differences should not be interpreted as uncertainties in ALL_RAD alone. The BMA-FLX product serves as a useful independent reference dataset based on BBR observations. Its TOA fluxes are retrieved from BBR multi-angle radiances through the BM-RAD unfiltering process (Velázquez Blázquez et al., 2024a) and the BMA-FLX radiance-to-flux conversion process using an angular distribution model (Velázquez Blázquez et al., 2024b). In addition, the comparison includes differences in spatial representativeness between the nadir-only sampling of ALL_RAD and the assessment-domain averages of BMA-FLX. Therefore, quantitatively separating the contributions from the cloud–radiation representation in ALL_RAD, the BMA-FLX retrieval process, and representativeness uncertainties associated with the comparison remains an important issue for future work.

The clear-sky comparison shown in Fig. 7 also suggests additional uncertainties that warrant further attention. In the SW clear-sky comparison, residual differences may be related to aerosol representation over ocean (Fig. 7a), whereas over land they appear to be associated mainly with surface properties (Fig. 7b). Because aerosol radiative effects are another important application target of ALL_RAD, further validation of aerosol representation remains important. In addition, the positive bias in clear-sky LW fluxes under low-temperature conditions (Figs. 7c and 7d) suggests the need to examine the uncertainties of input surface temperature data and their treatment in radiative transfer calculations, particularly over and around Antarctica.

The CRE and HR structures shown in Figs. 9 and 10 indicate that ALL_RAD can be used not only for radiative closure assessment, but also for analyzing cloud radiative effects and atmospheric radiative heating rates. Although uncertainties related to geographical patterns and cloud regimes remain in the ALL_RAD SW fluxes, they appear to be partly averaged out in the zonal-mean CREs, which are broadly consistent with those derived using BMA-FLX (Fig. 9a). The CREs at TOA, BOA, and within the atmosphere (Fig. 9), as well as the heating rates associated with cloud radiative effects (Fig. 10), are broadly compatible with existing physical understanding and previous studies based on CloudSat/A-Train observations (e.g., L'Ecuyer et al., 2008; Kato et al., 2018), and they reasonably represent the latitude–height structure of cloud-induced heating and cooling. Nevertheless, these analyses are based only on one month of data from August 2025, and longer-term analyses are essential for discussing seasonal variations, annual means, and climatological characteristics.

Future work can be broadly organized into two directions. The first is the expansion of validation datasets. The comparison with BMA-FLX should be extended to longer periods to quantify uncertainties depending on cloud regime, season, and region. Similarly, the comparison with BSRN ground-based observations should be expanded to include more sites and longer periods. In particular, ground-based sites that simultaneously observe radiative fluxes together with cloud and aerosol properties could provide more information from the limited matchup data. In addition, comparison with the ESA radiation product ACM-RT (Cole et al., 2024), the counterpart of ALL_RAD, would also help distinguish uncertainties common to both products from algorithm-specific uncertainties.

The second direction is the advancement of validation methodologies. ALL_RAD currently calculates radiative fluxes using cloud and aerosol information based on nadir observations. By applying a donor–recipient approach, as used in A-Train analyses (Barker et al., 2011; Okata et al., 2017), CPR/ATLID cloud vertical profiles observed along the nadir track could be assigned to across-track MSI pixels within the assessment domain. The resulting reconstructed three-dimensional cloud fields would be useful for evaluating representativeness uncertainties associated with nadir sampling in the ALL_RAD–BMA-FLX comparison. They could also be used as input for 3D radiative transfer calculations, which can provide multi-angle radiances. Direct comparison of these simulated radiances with BM-RAD radiances would enable a radiance-level evaluation of ALL_RAD, independent of the ADM-based flux conversion in BMA-FLX. This would complement the radiative closure assessment based on the BMA-FLX flux comparison.

The ESA operational products already include components for three-dimensional cloud-field reconstruction (ACMB-3D; Qu et al., 2023), 3D radiative transfer calculations (ACM-RT), and radiative closure assessment based on these calculations (ACMB-DF; Barker et al., 2025). For ALL_RAD, it will also be important to develop a framework that can quantify representativeness uncertainties and 3D radiative effects, in addition to the current nadir-based 1D radiative transfer calculations. This would allow the evaluation to go beyond the validation of TOA and surface fluxes and toward a more comprehensive assessment of cloud and aerosol radiative effects.

7 Conclusions

In this study, we conducted an initial evaluation of ALL_RAD version Ba, the JAXA four-sensor synergy radiation budget product, using actual EarthCARE observations. The ALL_RAD algorithm generates composite cloud and aerosol profiles by integrating JAXA Level-2 retrieval products derived from CPR, ATLID, and MSI, and then estimates broadband SW and LW radiative fluxes at the TOA and surface, as well as radiative heating-rate profiles, using a one-dimensional radiative transfer model. The performance of the ALL_RAD radiative flux estimates was evaluated through comparisons with the BBR-based BMA-FLX product at the TOA and ground-based BSRN observations at the surface.

The TOA radiative fluxes from ALL_RAD generally showed good agreement with BMA-FLX. In particular, LW fluxes showed small biases and RMSEs under both all-sky and clear-sky conditions, indicating stable performance. For SW fluxes, the overall mean bias was small and the RMSE remained within a reasonable range. Nevertheless, non-negligible cloud-regime-dependent biases and error SDs were identified, suggesting the need for further improvements in the ALL_RAD algorithm itself, together with continued refinement of the input Level-2 products. The improved agreement relative to pre-launch assessments reflects the maturation of the ALL_RAD algorithm together with improvements in the upstream EarthCARE Level-1 and Level-2 products.

For surface radiative fluxes, although the number of available BSRN matchups was limited, ALL_RAD broadly reproduced the variability of downward SW and LW surface fluxes. This provides initial evidence that ALL_RAD provides reasonable radiative flux estimates not only at the TOA but also at the surface. Further validation using more sites and longer periods is needed to obtain a more robust assessment.

As an application of the ALL_RAD radiative fluxes, we also analyzed cloud and aerosol radiative effects and cloud-induced radiative heating rates. These quantities showed latitudinal and latitude–height structures that were broadly consistent with existing physical understanding and previous studies based on A-Train observations. This indicates that ALL_RAD can provide useful information not only for radiative closure assessment, but also for analyzing radiative impacts of clouds and aerosols and atmospheric radiative heating rates.

Future work should extend the validation to longer periods and a wider range of regions and cloud regimes. Further evaluation of aerosol radiative effects is also needed, particularly through comparisons with observations that provide simultaneous information on aerosols and radiative fluxes. In addition, separating the ALL_RAD–BMA-FLX differences into contributions from uncertainties in the two products themselves, spatial representativeness, and three-dimensional radiative effects will be important for improving the interpretation of these differences and for advancing radiative closure assessment using EarthCARE observations.

Data availability

The EarthCARE products used in this study are available online on the Globe Portal System (G-Portal) of JAXA (https://gportal.jaxa.jp) and are identified by the following DOIs: EarthCARE L2B Four Sensor Synergy Radiation Budget Product (ALL_RAD; https://doi.org/10.57746/EO.01jkwjp98y6mndbxt887cgcgw6; JAXA, 2024a), EarthCARE L2B CPR-ATLID Synergy Cloud Products (AC_CLP; https://doi.org/10.57746/EO.01jkwjeg2y0bqndnsvjvaaskaw; JAXA, 2024b), EarthCARE L2A ATLID one-sensor Cloud Products (ATL_CLA; https://doi.org/10.57746/EO.01jkwjk45jrx9frz6c11x4rs8e; JAXA, 2024c), and EarthCARE L2A MSI one-sensor Cloud Products (MSI_CLP; https://doi.org/10.57746/EO.01jkwjkd9yt4shyz0z27drfve3; JAXA, 2024d). The two surface emissivity products, derived from the UW Baseline Fit Emissivity Database based on MODIS observations and the ASTER Global Emissivity Dataset, are available from the Cooperative Institute for Meteorological Satellite Studies (CIMSS), University of Wisconsin–Madison (https://cimss.ssec.wisc.edu/iremis/).

Author contribution

TMN: Formal analysis Methodology, Software, Visualization, Writing – original draft;
KS: Conceptualization, Funding acquisition, Supervision, Writing – review & editing;
AY: Methodology, Software, Writing – review & editing;
EO: Methodology, Software, Writing – review & editing;
MS: Methodology, Software, Writing – review & editing;
HI: Methodology, Software, Writing – review & editing;
MM: Resources, Data curation, Software, Writing – review & editing.
All authors have read and agreed to the submitted version of the manuscript.

Competing interests

One of the authors (K. Suzuki) serves as an Editor of the special issue "Early results from EarthCARE (AMT/ACP/GMD inter-journal SI)". The authors declare that they have no other conflicts of interest.

https://doi.org/10.5194/egusphere-2026-4324
Preprint. Discussion started: 13 August 2026

Acknowledgments

This manuscript was prepared with assistance from AI-tools for English editing and manuscript wording. The authors reviewed and revised all AI-assisted text and take full responsibility for the content of the manuscript.

Financial support

This study was supported by the Japan Aerospace Exploration Agency (JAXA) through the fourth Research Announcement on the Earth Observations (EO-RA4) for the EarthCARE mission and the MEXT program for the Advanced Studies of Climate Change Projection (SENTAN) (Grant JPMXD0722680395).

https://doi.org/10.5194/egusphere-2026-4324
Preprint. Discussion started: 13 August 2026

References

Barker, H. W., Jerg, M. P., Wehr, T., Kato, S., Donovan, D. P., and Hogan, R. J.: A 3D cloud-construction algorithm for the EarthCARE satellite mission, Q. J. R. Meteorol. Soc., 137, 1042–1058, https://doi.org/10.1002/qj.824, 2011.

Barker, H. W., Cole, J. N. S., Villefranque, N., Qu, Z., Blázquez, A. V., Domenech, C., Mason, S. L., and Hogan, R. J.: Radiative closure assessment of retrieved cloud and aerosol properties for the EarthCARE mission: the ACMB-DF product, Atmos. Meas. Tech., 18, 3095–3107, https://doi.org/10.5194/amt-18-3095-2025, 2025.

Cole, J. N. S., Barker, H. W., Qu, Z., Villefranque, N., and Shephard, M. W.: Broadband radiative quantities for the EarthCARE mission: the ACM-COM and ACM-RT products, Atmos. Meas. Tech., 16, 4271–4288, https://doi.org/10.5194/amt-16-4271-2023, 2023.

Eisinger, M., Marnas, F., Wallace, K., Kubota, T., Tomiyama, N., Ohno, Y., Tanaka, T., Tomita, E., Wehr, T., and Bernaerts, D.: The EarthCARE mission: science data processing chain overview, Atmos. Meas. Tech., 17, 839–862, https://doi.org/10.5194/amt-17-839-2024, 2024.

Ham, S., Kato, S., Rose, F. G., Winker, D., L'Ecuyer, T., Mace, G. G., Painemal, D., Sun-Mack, S., Chen, Y., and Miller, W. F.: Cloud occurrences and cloud radiative effects (CREs) from CERES-CALIPSO-CloudSat-MODIS (CCCM) and CloudSat radar-lidar (RL) products, J. Geophys. Res.: Atmos., 122, 8852–8884, https://doi.org/10.1002/2017jd026725, 2017.

Hartmann, D. L. and Short, D. A.: On the Use of Earth Radiation Budget Statistics for Studies of Clouds and Climate, J. Atmos. Sci., 37, 1233–1250, https://doi.org/10.1175/1520-0469(1980)037<1233:otuoer>2.0.co;2, 1980.

Henderson, D. S., L'Ecuyer, T., Stephens, G., Partain, P., and Sekiguchi, M.: A Multisensor Perspective on the Radiative Impacts of Clouds and Aerosols, J. Appl. Meteorol. Climatol., 52, 853–871, https://doi.org/10.1175/jamc-d-12-025.1, 2013.

Hulley, G. C., Hook, S. J., Abbott, E., Malakar, N., Islam, T., and Abrams, M.: The ASTER Global Emissivity Dataset (ASTER GED): Mapping Earth's emissivity at 100 meter spatial scale, Geophys. Res. Lett., 42, 7966–7976, https://doi.org/10.1002/2015gl065564, 2015.

Illingworth, A. J., Barker, H. W., Beljaars, A., Ceccaldi, M., Chepfer, H., Clerbaux, N., Cole, J., Delanoë, J., Domenech, C., Donovan, D. P., Fukuda, S., Hirakata, M., Hogan, R. J., Huenerbein, A., Kollias, P., Kubota, T., Nakajima, T., Nakajima, T. Y., Nishizawa, T., Ohno, Y., Okamoto, H., Oki, R., Sato, K., Satoh, M., Shephard, M. W., Velázquez-Blázquez, A., Wandinger, U., Wehr, T., and Zadelhoff, G.-J. van: The EarthCARE Satellite: The Next Step Forward in Global Measurements of Clouds, Aerosols, Precipitation, and Radiation, Bull. Am. Meteorol. Soc., 96, 1311–1332, https://doi.org/10.1175/bams-d-12-00227.1, 2015.

Ishimoto, H., Masuda, K., Mano, Y., Orikasa, N., and Uchiyama, A.: Irregularly shaped ice aggregates in optical modeling of convectively generated ice clouds, J Quantitative Spectrosc Radiat Transf, 113, 632–643, https://doi.org/10.1016/j.jqsrt.2012.01.017, 2012.

https://doi.org/10.5194/egusphere-2026-4324
Preprint. Discussion started: 13 August 2026

IPCC: Climate Change 2023: Synthesis Report. Contribution of Working Groups I, II and III to the Sixth Assessment Report of the Intergovernmental Panel on Climate Change [Core Writing Team, H. Lee and J. Romero (eds.)]. IPCC, Geneva, Switzerland., https://doi.org/10.59327/ipcc/ar6-9789291691647, 2023.

JAXA: EarthCARE L2B Four-sensors Synergy Radiative Products, https://doi.org/10.57746/EO.01jkwjp98y6mndbxt887cgcgw6, 2024a.

JAXA: EarthCARE L2B CPR-ATLID Synergy Cloud Products, https://doi.org/10.57746/EO.01jkwjeg2y0bqndnsvjvaaskaw, 2024b.

JAXA: EarthCARE/ATLID L2A ATLID one-sensor Cloud Aerosol Products, https://doi.org/10.57746/EO.01jkwjk45jrx9frz6c11x4rs8e, 2024c.

JAXA: EarthCARE/MSI L2A MSI one-sensor Cloud Products, https://doi.org/10.57746/EO.01jkwjkd9yt4shyz0z27drfve3, 2024d.

JAXA: EarthCARE JAXA Level 2 Algorithm Theoretical Basis Document, Japan Aerospace Exploration Agency, available at: https://www.eorc.jaxa.jp/EARTHCARE/document/JAXAL2ProductList/ATBD/EarthCARE_JAXA_L2_ATBD_verP_Apr2026.pdf, last access: 23 June 2026, 2026.

Kato, S., Rose, F. G., Sun-Mack, S., Miller, W. F., Chen, Y., Rutan, D. A., Stephens, G. L., Loeb, N. G., Minnis, P., Wielicki, B. A., Winker, D. M., Charlock, T. P., Stackhouse, P. W., Xu, K., and Collins, W. D.: Improvements of top-of-atmosphere and surface irradiance computations with CALIPSO-, CloudSat-, and MODIS-derived cloud and aerosol properties, J. Geophys. Res.: Atmos., 116, https://doi.org/10.1029/2011jd016050, 2011.

Kato, S., Rose, F. G., Ham, S. H., Rutan, D. A., Radkevich, A., Caldwell, T. E., Sun-Mack, S., Miller, W. F., and Chen, Y.: Radiative Heating Rates Computed With Clouds Derived From Satellite-Based Passive and Active Sensors and their Effects on Generation of Available Potential Energy, J. Geophys. Res.: Atmos., 124, 1720–1740, https://doi.org/10.1029/2018jd028878, 2018.

L'Ecuyer, T. S., Wood, N. B., Haladay, T., Stephens, G. L., and Stackhouse, P. W.: Impact of clouds on atmospheric heating based on the R04 CloudSat fluxes and heating rates data set, J. Geophys. Res.: Atmos., 113, https://doi.org/10.1029/2008jd009951, 2008.

L'Ecuyer, T. S., Beaudoing, H. K., Rodell, M., Olson, W., Lin, B., Kato, S., Clayson, C. A., Wood, E., Sheffield, J., Adler, R., Huffman, G., Bosilovich, M., Gu, G., Robertson, F., Houser, P. R., Chambers, D., Famiglietti, J. S., Fetzer, E., Liu, W. T., Gao, X., Schlosser, C. A., Clark, E., Lettenmaier, D. P., and Hilburn, K.: The Observed State of the Energy Budget in the Early Twenty-First Century, J Climate, 28, 8319–8346, https://doi.org/10.1175/jcli-d-14-00556.1, 2015.

Letu, H., Nakajima, T. Y., and Matsui, T. N.: Development of an ice crystal scattering database for the global change observation mission/second generation global imager satellite mission: investigating the refractive index grid system and potential retrieval error, Appl Optics, 51, 6172, https://doi.org/10.1364/ao.51.006172, 2012.

https://doi.org/10.5194/egusphere-2026-4324
Preprint. Discussion started: 13 August 2026

Letu, H., Ishimoto, H., Riedi, J., Nakajima, T. Y., Labonnote, L. C., Baran, A. J., Nagao, T. M., and Sekiguchi, M.: Investigation of ice particle habits to be used for ice cloud remote sensing for the GCOM-C satellite mission, Atmos. Chem. Phys., 16, 12287–12303, https://doi.org/10.5194/acp-16-12287-2016, 2016.

Liebmann, B. and Hartmann, D. L.: Interannual Variations of Outgoing IR Associated with Tropical Circulation Changes During 1974–78, J. Atmos. Sci., 39, 1153–1162, https://doi.org/10.1175/1520-0469(1982)039<1153:IVOOIA>2.0.CO;2, 1982.

Loeb, N. G., Doelling, D. R., Wang, H., Su, W., Nguyen, C., Corbett, J. G., Liang, L., Mitrescu, C., Rose, F. G., and Kato, S.: Clouds and the Earth's Radiant Energy System (CERES) Energy Balanced and Filled (EBAF) Top-of-Atmosphere (TOA) Edition 4.0 Data Product, J. Clim., 31, 895–918, https://doi.org/10.1175/jcli-d-17-0208.1, 2018.

Luo, H., Quaas, J., and Han, Y.: Examining cloud vertical structure and radiative effects from satellite retrievals and evaluation of CMIP6 scenarios, Atmos. Chem. Phys., 23, 8169–8186, https://doi.org/10.5194/acp-23-8169-2023, 2023.

Matus, A. V. and L'Ecuyer, T. S.: The role of cloud phase in Earth's radiation budget, J Geophys Res Atmospheres, 122, 2559–2578, https://doi.org/10.1002/2016jd025951, 2017.

Matus, A. V., L'Ecuyer, T. S., and Henderson, D. S.: New Estimates of Aerosol Direct Radiative Effects and Forcing From A-Train Satellite Observations, Geophys. Res. Lett., 46, 8338–8346, https://doi.org/10.1029/2019gl083656, 2019.

Nakajima, T., Tsukamoto, M., Tsushima, Y., Numaguti, A., and Kimura, T.: Modeling of the radiative process in an atmospheric general circulation model, Appl. Opt., 39, 4869–4878, https://doi.org/10.1364/ao.39.004869, 2000.

Nishizawa, T., Kudo, R., Oikawa, E., Higurashi, A., Jin, Y., Sugimoto, N., Sato, K., and Okamoto, H.: Algorithms to retrieve aerosol optical properties using lidar measurements on board the EarthCARE satellite, Atmos. Meas. Tech., 19, 729–744, https://doi.org/10.5194/amt-19-729-2026, 2026.

Ohmura, A., Gilgen, H., Hegner, H., Müller, G., Wild, M., Dutton, E. G., Forgan, B., Fröhlich, C., Philipona, R., Heimo, A., König-Langlo, G., McArthur, B., Pinker, R., Whitlock, C. H., and Dehne, K.: Baseline Surface Radiation Network (BSRN/WCRP): New Precision Radiometry for Climate Research, Bull. Am. Meteorol. Soc., 79, 2115–2136, https://doi.org/10.1175/1520-0477(1998)079<2115:bsrnbw>2.0.co;2, 1998.

Oikawa, E., Nakajima, T., Inoue, T., and Winker, D.: A study of the shortwave direct aerosol forcing using ESSP/CALIPSO observation and GCM simulation, J. Geophys. Res.: Atmos., 118, 3687–3708, https://doi.org/10.1002/jgrd.50227, 2013.

Oikawa, E., Nakajima, T., and Winker, D.: An Evaluation of the Shortwave Direct Aerosol Radiative Forcing Using CALIOP and MODIS Observations, J. Geophys. Res.: Atmos., 123, 1211–1233, https://doi.org/10.1002/2017jd027247, 2018.

Okata, M., Nakajima, T., Suzuki, K., Inoue, T., Nakajima, T. Y., and Okamoto, H.: A study on radiative transfer effects in 3-D cloudy atmosphere using satellite data, J. Geophys. Res.: Atmos., 122, 443–468, https://doi.org/10.1002/2016jd025441, 2017.

Qu, Z., Barker, H. W., Cole, J. N. S., and Shephard, M. W.: Across-track extension of retrieved cloud and aerosol properties for the EarthCARE mission: the ACMB-3D product, Atmos. Meas. Tech., 16, 2319–2331, https://doi.org/10.5194/amt-16-2319-2023, 2023.

https://doi.org/10.5194/egusphere-2026-4324
Preprint. Discussion started: 13 August 2026

Sato, K., Okamoto, H., Nishizawa, T., Jin, Y., Nakajima, T. Y., Wang, M., Satoh, M., Roh, W., Ishimoto, H., and Kudo, R.: JAXA Level 2 cloud and precipitation microphysics retrievals based on EarthCARE radar, lidar, and imager: the CPR_CLP, AC_CLP, and ACM_CLP products, Atmos. Meas. Tech., 18, 1325–1338, https://doi.org/10.5194/amt-18-1325-2025, 2025.

Seemann, S. W., Borbas, E. E., Knuteson, R. O., Stephenson, G. R., and Huang, H.-L.: Development of a Global Infrared Land Surface Emissivity Database for Application to Clear Sky Sounding Retrievals from Multispectral Satellite Radiance Measurements, J. Appl. Meteorol. Climatol., 47, 108–123, https://doi.org/10.1175/2007jamc1590.1, 2008.

Sekiguchi, M. and Nakajima, T.: A k-distribution-based radiation code and its computational optimization for an atmospheric general circulation model, J. Quant. Spectrosc. Radiat. Transf., 109, 2779–2793, https://doi.org/10.1016/j.jqsrt.2008.07.013, 2008.

Stephens, G. L., Li, J., Wild, M., Clayson, C. A., Loeb, N., Kato, S., L'Ecuyer, T., Stackhouse, P. W., Lebsock, M., and Andrews, T.: An update on Earth's energy balance in light of the latest global observations, Nat Geosci, 5, 691–696, https://doi.org/10.1038/ngeo1580, 2012.

Stephens, G. L., O'Brien, D., Webster, P. J., Pilewski, P., Kato, S., and Li, J.: The albedo of Earth: The Albedo of Earth, Rev Geophys, 53, 141–163, https://doi.org/10.1002/2014rg000449, 2015.

Stephens, G., Winker, D., Pelon, J., Trepte, C., Vane, D., Yuhas, C., L'Ecuyer, T., and Lebsock, M.: CloudSat and CALIPSO within the A-Train: Ten Years of Actively Observing the Earth System, B Am Meteorol Soc, 99, 569–581, https://doi.org/10.1175/bams-d-16-0324.1, 2018.

Velázquez Blázquez, A. V., Baudrez, E., Clerbaux, N., and Domenech, C.: Unfiltering of the EarthCARE Broadband Radiometer (BBR) observations: the BM-RAD product, Atmos. Meas. Tech., 17, 4245–4256, https://doi.org/10.5194/amt-17-4245-2024, 2024a.

Velázquez Blázquez, A. V., Domenech, C., Baudrez, E., Clerbaux, N., Molar, C. S., and Madenach, N.: Retrieval of top-of-atmosphere fluxes from combined EarthCARE lidar, imager, and broadband radiometer observations: the BMA-FLX product, Atmos. Meas. Tech., 17, 7007–7026, https://doi.org/10.5194/amt-17-7007-2024, 2024b.

Wang, M., Nakajima, T. Y., Roh, W., Satoh, M., Suzuki, K., Kubota, T., and Yoshida, M.: Evaluation of the spectral misalignment on the Earth Clouds, Aerosols and Radiation Explorer/multi-spectral imager cloud product, Atmos. Meas. Tech., 16, 603–623, https://doi.org/10.5194/amt-16-603-2023, 2023.

Wehr, T., Kubota, T., Tzeremes, G., Wallace, K., Nakatsuka, H., Ohno, Y., Koopman, R., Rusli, S., Kikuchi, M., Eisinger, M., Tanaka, T., Taga, M., Deghaye, P., Tomita, E., and Bernaerts, D.: The EarthCARE mission – science and system overview, Atmos. Meas. Tech., 16, 3581–3608, https://doi.org/10.5194/amt-16-3581-2023, 2023.

Yamauchi, A., Suzuki, K., Oikawa, E., Sekiguchi, M., Nagao, T. M., and Ishida, H.: Description and validation of the Japanese algorithm for radiative flux and heating rate products with all four EarthCARE instruments: pre-launch test with A-Train, Atmos. Meas. Tech., 17, 6751–6767, https://doi.org/10.5194/amt-17-6751-2024, 2024.